# Thermoacoustic Instabilities in Counterflow Diffusion Flames

by

Matthew Yao

A thesis
presented to the University of Waterloo
in fulfillment of the
thesis requirement for the degree of
Master of Applied Science
in
Mechanical & Mechatronics Engineering

Waterloo, Ontario, Canada, 2019

# Author's Declaration

I hereby declare that I am the sole author of this thesis. This is a true copy of the thesis, including any required final revisions, as accepted by my examiners.

I understand that my thesis may be made electronically available to the public.

## Abstract

Thermoacoustic instabilities arise in combustion systems from a coupling between the unsteady heat release of the flame and the underlying acoustic field. Although thermoacoustics have been studied extensively with regards to premixed flames, where the fuel and oxidizer are fully mixed before combustion, the study of thermoacoustics in diffusion flames is much more limited. However, thermoacoustic instabilities are also of interest for the design of systems which are better characterized by diffusion or nonpremixed flames, for example, liquid rocket engines. As such, this thesis aims to investigate, using an in-house developed combustion solver, the behaviour of thermoacoustic fluctuations in a diffusion flame.

The thermoacoustics are studied in the counterflow diffusion flame configuration, where the flame exists between two opposed jets containing the fuel and oxidizer respectively. An unsteady compressible reactive flow solver is integrated into an in-house code. The code is then coupled to Cantera to obtain the transport and thermodynamic properties. Finally, to study the thermoacoustics, time-dependent Navier-Stokes Characteristic Boundary Conditions are implemented in the code to account for fully reflecting, partially reflecting, and nonreflecting boundary conditions. The code is validated against the steady solution obtained from Cantera.

The flame under consideration consists of $H_2$ as the fuel and a mixture of $O_2$ and $N_2$ as the oxidizer. Two different strain rates are studied. Under the assumption of perfectly reflecting boundary conditions, the growth of the acoustic perturbations in the high strain rate case is much more significant than the low strain rate case. Under the partially reflecting boundary conditions, the high strain rate case also exhibits some slight growth of the acoustic perturbations. An underlying standing wave behaviour can be identified and the dominants modes extracted through a spectral analysis. For further investigation, a number of forced sinusoidal pulses were introduced into the fuel stream, and the response was measured via Rayleigh's criterion. The results show that the acoustic fluctuations are amplified for a larger range of frequencies in the high strain rate case compared to the low strain rate case, which helps to explain why the acoustic growth in the high strain rate case is much more significant.

**Acknowledgements**

I would first like to extend my gratitude to my supervisor Prof. Jean-Pierre Hickey. Your constant guidance and support has always been an inspiration to me, even when I did not see the light myself. You've taught me many lessons about research and life which I will carry with me as I progress in my career. I would like to thank the people in our research group for their interesting discussions, both regarding research and not. I am also grateful to NSERC and the University of Waterloo for their financial support, allowing me to pursue my research interests.

I would also like to thank my parents for their unconditional support and love. You have given me the confidence to pursue my dreams and I cannot thank you enough. Thank you to my grandma for her delicious cooking to keep me going. Thank you to my siblings Kathleen and David for always being my cheerleaders.

I would like to thank my friends from Waterloo. Dionne, Brian, Shan, Ned, Suyeon, Savannah, and Omar, you guys have made my time at Waterloo the most enjoyable.

Finally, I would like to thank my girlfriend Jessica. You are my rock and I could not have made it this far without you.

## Dedication

This is dedicated to Jessica, whose unwavering support has been instrumental in keeping me focused throughout my studies. I love you.

# Table of Contents

# List of Tables

# List of Figures

# Abbreviations

**EoS** equation of state 16, 50

**ITA** intrinsic thermoacoustic 2

**NSCBC** Navier-Stokes Characteristic Boundary Conditions 18, 26, 31, 33, 37, 45

# Chapter 1

# Introduction

First explained by Lord Rayleigh [53], thermoacoustic instabilities arise from the interaction between the unsteady heat release of the flame and the underlying acoustic field. This coupling can create large amplitude oscillations [45], which can result in deleterious effects such as noise generation or, in more severe cases, fatigue or excessive heat transfer to the combustor walls [43]. The thermoacoustic instabilities are often a direct result of the geometry of the combustion system. The typical mechanism is described as follows [24]. First, the unsteady heat release acts as a source of noise and creates acoustic waves which reflect off of the various components of the combustor chamber, for example, the walls or the plenum. Then, the reflected acoustic waves can modulate the flow conditions and perturb the flame. This creates an unsteady heat release thereby closing the feedback loop. Self-excitation of the acoustic waves can occur if the correlation between the pressure and the heat release fluctuations are favorable, a condition which is now referred to as Rayleigh's criterion [24, 45]. For the one-dimensional laminar flamelets under a sine wave acoustic perturbation, Rayleigh's criterion can be expressed mathematically in terms of an amplification factor $H$ [65]:

$$H = \frac{1}{\tau} \int_0^\tau \frac{Q - Q_m}{Q_m} \sin(2\pi f t) \mathrm{d}t \tag{1.1}$$

where $Q$ is the heat release rate, $\tau$ is the acoustic period, $f$ is the frequency, and $t$ is the time. The subscript $m$ refers to the mean heat release, or the steady heat release with no effects of acoustic forcing. If the phase angle between the acoustic pressure and the heat release is between $-90°$ and $90°$, then acoustic amplification is predicted [65].

Although thermoacoustic instabilities have been a problem for rocket engine design since the early 1930s, recently, the study of thermoacoustic instabilities has become more

relevant and important for low emission gas turbine design [32]. Modern gas chambers are designed with increasingly strict limits on pollutant emissions such as, $NO_x$. As such, the design principles have changed, and for a variety of reasons, the design of modern, low emission gas turbines results in combustor walls which have very little attenuation of noise [32]. Thus, from both a theoretical and practical point of view, understanding the onset and propagation of thermoacoustic oscillations and instabilities is very relevant in the context of modern day engineering applications.

Although the classical view is that the thermoacoustic instabilities are dependent on the geometry and acoustic modes of the system, recently researchers have discovered the existence of intrinsic thermoacoustic (ITA) instabilities, in which the feedback loop is closed and thermoacoustic oscillations are sustained with no dependence on the combustor geometry [13, 23, 24, 26, 59, 60, 79]. These ITA instabilities are identified in the case of premixed combustion, in which the fuel and oxidizer are fully mixed before combustion. Experimental and numerical results show that even under the conditions of highly anechoic boundary conditions, these instabilities can propagate purely based on the coupling between the unsteady heat release and the flow field. The main reason that thermoacoustic instabilities are of primary interest in premixed flames is that they are very sensitive to velocity perturbations [9]. In these cases, the velocity perturbations result in fluctuations in the heat release which generate acoustic waves. Due to the sensitivity to velocity perturbations in premixed flames, the acoustic waves may be sufficient to alter the velocity field and close the feedback loop. In this way, ITA instabilities are independent of the combustor geometry and are of specific interest to the combustion community.

Most of the research on thermoacoustics is focused on the premixed flame. However, in many applications, the diffusion (or partially pre-mixed) flames may be a more realistic description of the combustion process. For example, in turbulent combustion, oftentimes the turbulent flame is considered to be an ensemble of laminar diffusion flamelets [49]. The model is particularly well-suited for reactive flows with a large scale separation between the timescales of transport phenomena and chemical reactions; the ratio of these timescales represents the Damkölher number. High Damkölher number reactive flows are particularly prevalent in liquid rocket engines, since the higher pressures tend to reduce the flame thickness [64] and, concurrently, reduce the time scales of the reaction. For example, recent experimental results from researchers at DLR [1] have shown presence of self-excited, high-frequency acoustic instabilities in high-pressure liquid rocket engines. As such, it is important to study the thermoacoutic properties and behaviour for diffusion flames as well. Although many practical applications are very complex, the simplified model of the counterflow diffusion flame allows us to isolate specific aspects of interest to study in detail. The one-dimensional counterflow diffusion flame allows us to fully resolve all of the acoustics in

order to isolate the fundamental physics of the problem. Despite thermoacoustic instabilities typically being three-dimensional, there are many factors which render the problem very computationally expensive, for example, the large number of species transport equations used for heavier fuels. To reduce the complexity of modelling the thermoacoustics, typically researchers introduce the flame transfer function which acts as a black box and represents the response of the flame to velocity perturbations. The heat release rate, $Q$, and upstream velocity perturbations, $u_u$, are related through the flame transfer function $F(s)$ as [24]:

$$\frac{Q'}{Q} = F(s)\frac{u'_u}{u_u} \tag{1.2}$$

where the prime denotes a fluctuation. The flame transfer function can be obtained experimentally or theoretically [19]. The flame transfer function is a useful model for premixed flames. One of the defining characteristics of premixed flames is the laminar flame speed, which determines how fast the flame propagates throughout the mixture. Because the fuel and oxidizer are fully mixed, the limiting factor for the premixed flame is the chemical reaction timescale. Because of this, a small velocity perturbation may directly influence the location and total heat release of the flame, creating the onset of instabilities. In this sense, the premixed flame is highly sensitive to velocity perturbations. It follows that the flame transfer function is a technique which is used to model premixed combustors only. However, thermoacoustic oscillations may also arise in diffusion flames for which there is little to no literature regarding an analogous flame transfer function. For the diffusion flame, the fuel and oxidizer must first undergo mass transfer and diffuse into each other before a reaction can take place. In this case, the unsteady heat release may not be directly sensitive to the velocity fluctuations as in the case of the premixed flame, and the response of the flame to velocity perturbations is diffusion limited [22]. Instead, the pressure fluctuations may impact the chemical mechanism and affect the production of certain species, an effect which has been studied by Sohn and Sung [63]. The aim of this thesis is to investigate thermoacoustics in the canonical counterflow diffusion flame configuration to simplify the problem and study the fundamental behaviour of the thermoacoustic fluctuations.

The remainder of the thesis is structured as follows. Chapter 2 presents the background on counterflow diffusion flames and introduces some of the relevant literature. Chapter 3 presents the governing equations and mathematical formulation of the problem, including the governing equations and the boundary conditions. The numerical details and the development of the code are also discussed. Chapter 4 presents the results of the thesis, which include results on strain rate, boundary conditions, and an analysis of traveling pressure waves. Finally, the conclusions are presented in Chapter 5, with discussions for

how to extend the work in the future.

## 1.1 Contributions of the thesis

The main contributions of the thesis can be summarized as follows:

- Development and validation of a reactive flow solver for 1D counterflow diffusion flames with time dependent boundary conditions
- Integration of the high-pressure Cantera kinetic package to the computation of the 1D flame
- Study the boundary condition effects on the self-sustaining thermoacoustic instability
- Evaluate the thermoacoustic behaviour for a propagating pressure wave
- First study of self sustaining thermoacoustic oscillations in a flame with a large density gradient
- Investigate strain rate effects on the behaviour of the thermoacoustic waves

# Chapter 2

# Background

## 2.1 Counterflow Diffusion Flame

The counterflow diffusion flame is a laminar flame which is dependent on the diffusion only and, as such, is a pure diffusion flame [74]. In his review paper, Tsuji [74] describes four different canonical cases for the counterflow diffusion flame; however, nowadays the most commonly referred to case is the opposed jet configuration, in which the fuel and oxidizer impinge upon each other at the stagnation plane between the two round jets. A schematic diagram of the counterflow diffusion flame is shown in Figure 2.1. Note that the flame sheet and the stagnation plane are not necessarily coincident, as the location of the flame depends on the diffusion and composition of the fuel and oxidizer within the mixture. The mathematical formulation of the counterflow diffusion flame is presented in Chapter 3.

Some important parameters governing the counterflow diffusion flame are the inlet compositions, temperatures, and velocities. The counterflow configuration is also typically referred to as 'strained', as the fuel and oxidizer streams are strained against each other. The strain rate is commonly used to characterise the flame. In this thesis, we refer to the strain rate $a$ as the global strain rate, which is calculated as the velocity difference of the two injectors divided by the separation distance [38]:

$$a = \frac{|u_{fuel}| + |u_{oxidizer}|}{L} \tag{2.1}$$

where $u$ is the inlet velocity and $L$ is the separation distance. Note that this is not the only definition of strain rate; in some cases it may be beneficial to study the local strain rate,

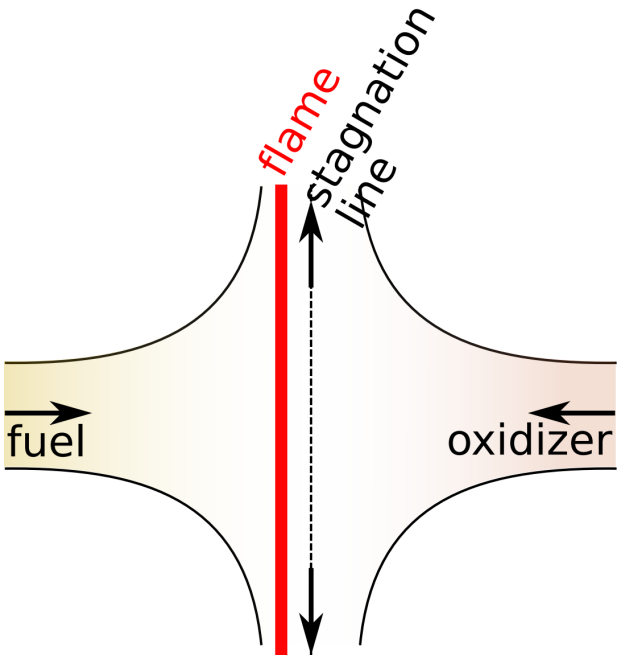


Figure 2.1: Schematic diagram of the laminar counterflow diffusion flame.

which can be considered as the velocity gradient $a = -\mathrm{d}u/\mathrm{d}x$ upstream from the thermal mixing layer on the oxidizer side [12, 78] or the velocity gradient at the fuel boundary [55]. The strain rate affects the overall flame structure; however, one of the key parameters is the extinction strain rate. In some cases, where the velocity of the inlets is too large, the flame may not be able to sustain itself and will extinguish as a result. Typically this occurs when the characteristic time scale of the rate of strain is smaller than the characteristic chemical reaction timescale. The corresponding strain rate is deemed to be the extinction strain rate. Typically, the heavier the fuel, the lower the extinction strain rate. The extinction strain rate is also dependent on the nozzle separation distance and increases as the separation distance is increased [20]. Additionally, a higher strain rate also leads to a thinner diffusive region and flame.

Over the years, the counterflow diffusion flame has garnered a significant amount of interest for a number of reasons. The simplicity of the problem allows one to isolate specific physical phenomena of interest, for example, studying the effects of strain rate [71], pressure [55], reduced chemical mechanisms [8], supercritical thermodynamics [4, 27, 30, 46], phase stability in supercritical combustion [73], and differential diffusion effects in combustion with real-gas effects [36, 50]. The concepts of flamelets have also been applied

to turbulent combustion simulations [49] where the turbulent flame is approximated as a collection of laminar flamelets.

To characterise the progression of the diffusion flame, a variable called the mixture fraction ($z$) is introduced. The mixture fraction is a scalar which represents, in a simplified form, the ratio of fuel versus oxidizer at any point in the flame. In the pure oxidizer stream, $z = 0$, and in the pure fuel stream, $z = 1$. In this work we define the mixture fraction for the $H_2$-$O_2$ flames as a passive scalar based on the H atom [52]:

$$z = W_{\mathrm{H}} \left( 2\frac{Y_{\mathrm{H_2}}}{W_{\mathrm{H_2}}} + \frac{Y_{\mathrm{H}}}{W_{\mathrm{H}}} + 2\frac{Y_{\mathrm{H_2O}}}{W_{\mathrm{H_2O}}} + \frac{Y_{\mathrm{OH}}}{W_{\mathrm{OH}}} + \frac{Y_{\mathrm{HO_2}}}{W_{\mathrm{HO_2}}} + 2\frac{Y_{\mathrm{H_2O_2}}}{W_{\mathrm{H_2O_2}}} \right) \tag{2.2}$$

Although the mixture fraction can be defined by the mass fractions of the fuel and oxidizer, by defining the mixture fraction as a passive scalar based on the elemental mass fractions we can account for the effect of multiple intermediate reactions and for unequal molecular diffusivities. For other fuels including hydrocarbons, for example, methane, the mixture fraction may be defined as a passive scalar based on the H and C atoms. The benefit of the mixture fraction is that it normalizes the mapping of the flame and removes the dependence on physical space to simplify comparisons between various operating conditions.

## 2.2 Literature Review

The unsteady counterflow diffusion flame has been the subject of many studies in the past [17, 20, 29, 37, 47, 70]. Typical studies aim to elucidate the unsteady effects of the flame through external forcing by introducing sinusoidal waves at the inlets. If $\phi$ is the variable of interest (for example, the inlet velocity), then the unsteadiness is introduced as:

$$\phi = \phi_m + \phi_a \sin(2\pi f t) \tag{2.3}$$

where the subscript $m$ denotes the time-averaged mean value and the subscript $a$ denotes the oscillation amplitude. The frequency $f$ is related to the angular frequency by $\omega = 2\pi f$ and $t$ is the time. The most commonly modified variable is the inlet velocity, which corresponds to a varying or unsteady strain rate.

Egolfopoulos and Campbell [22] studied the frequency response of the counterflow diffusion flame by varying the velocity, temperature, and composition of the inlets for a methane/air diffusion flame. They showed that for low frequencies, the flame follows the

externally forced oscillations in a quasi-steady manner, and at higher frequencies, the induced oscillations of the flame are attenuated and phase shifted. The reduced amplitude of the response is consistent with previous experimental results by Saitoh and Otsuka [56]. Interestingly, at the highest frequencies studied, the flame no longer responds to the forced oscillations. The study was further extended by Egolfopoulos [21] to study the effects of imposed oscillations on the extinction and re-ignition characteristics of the flame. At a low velocity frequency of 1 Hz, the diffusive and convective profiles of fuel and oxidizer are significantly different between the trough and peak profiles, meaning that the oscillations propagate through the diffusive zones and as such, directly affect the flame. However, at a higher frequency of 2000 Hz, the trough and peak profiles collapse in the diffusive zone, meaning that the imposed oscillations do not directly affect the heat release or burning rate. A study by Darabiha [16] showed that for strain rates far below the extinction strain rate, the flame response is linear, but for strain rates near the extinction strain rate, the response becomes nonlinear.

Studies by Cuoci *et al.* [14, 15] investigated the coupling between the chemistry and the sinusoidal velocity oscillation. In this case, their goal was to investigate the effect of unsteadiness on the pollutant formation of methane and propane flames. Similar to the previous work, they identified upper limits on the frequency at which the flame would respond. The main finding is that cut-off frequency is dependent on the timescale of the chemical reactions; if the frequency was too high then the chemistry was not able to respond to the strain rate oscillations. The cut-off frequency was found to be dependent on the global strain rate but not the oscillation amplitudes. These results are consistent with earlier findings by Xiao *et al.* [76], who showed experimentally that the pollutant formation fails to respond to high frequency velocity oscillations for methane and propane.

Although the previous studies have given us insight on the coupling between the fluid mechanics and the combustion process, one major drawback is that they do not consider the effects of pressure oscillations. In the simulations, the pressure oscillations are assumed to be small, and as such the pressure is assumed to have no spatial variation and the temporal term, $\partial p/\partial t$, in the energy equation is neglected. However, as noted by Egolfopoulos [21], at the higher frequencies ($f = 2000$ Hz), the acoustic pressure effects may become important, and in a complete study, the effects of pressure variation should be included. In the context of thermoacoustic instabilities, the inclusion of the unsteady pressure effects is especially important.

The earliest studies on the interaction of acoustic interactions with laminar flames were conducted in the 1960's by Strahle [66, 67, 68, 69]. The flames under consideration were not of the counterflowing configuration; instead, they were focused on reacting boundary layers or jet diffusion flames. The main limitation of these early studies is that they are

conducted under the assumption of infinitely fast chemistry. Since the dominant nonlinear term of the combustion process arises from the finite-rate chemistry [34], the importance of the coupling between the acoustics and the chemistry was not studied.

To bridge the gap and introduce the effects of finite-rate chemistry, Kim and Williams [34] conducted one of the earliest studies on acoustic pressure responses of counterflow diffusion flames. Their study is analytical, and they employ the technique of activation-energy asymptotics [75] which characterises a one-step Arrhenius-type reaction. According to the theory of activation-energy, the counterflow diffusion flame consists of a thin reactive-diffusive layer surrounded by convective-diffusive layers on either side [34], which allows for different characteristic length and time scales to be extracted. Based on their analysis of the linear acoustic response, they show that the linear response can be attributed to two main mechanisms [34]. The first is the fluctuation of the reaction sheet due to the acoustically modulated reaction rate fluctuations. This mechanism is found to be dominant when the strain rate of the flame is near the extinction strain rate. The second is oscillations of the field variables. This mechanism is found to be dominant for near-equilibrium flames. The overall conclusion is that amplification of the acoustic waves is largest near extinction strain rates.

The study of acoustics in counterflow diffusion flames was further extended by Sohn *et al.* [64] through numerical simulations of hydrogen and oxygen flames at high pressures using a mechanism of 8 species and 19 reactions. To close the governing equations at high pressures, they employ the Soave-Redlich-Kwong equation of state [62]. The response of the flame to acoustic perturbations is studied by imposing sinusoidal pressure oscillations, with amplitudes from 5-30% of the mean pressure value. They show that variation of the maximum flame temperature is largest at the trough pressure values. A more specific study on the dependence of the mean pressure was carried out by Sohn and Sung [63], in which they demarcated three extinction regimes dependent on the pressure. The first is where the extinction strain rate increases with pressure, the second is where the extinction strain rate decreases with pressure, and finally, the third consists of any flames at even higher pressures. In each regime, the effects of pressure on the heat release of the intermediate reactions is studied with respect to Rayleigh's criterion. A pressure increase results in an increase of the heat release due to the increase in branching and recombination reaction rates in the low pressure regime and the radical rebranching of $H_2O_2$ in the high pressure regime. As such, large acoustic amplifications are predicted in these regimes. In the medium pressure regime, only a weak or neutral amplification of the acoustic pressure waves is predicted. A final extension of the work was conducted by Sohn [65], in which the full unsteady conservation equations are solved with oscillating pressures. At low pressures and low frequencies, the amplification index is small; however, when the frequency is increased,

the amplification index becomes large due to an accumulation of the nonlinear response of the heat release rate. Similar to the studies without consideration of the acoustic pressure oscillations, the flame response is decreased at high frequencies as the flame fails to respond. At medium pressures and low frequencies, the amplification index is small, decreases with increasing frequency, and then increases with a further increasing frequency.

These studies on thermoacoustic instabilities are based on Rayleigh's criterion and an imposition of pressure fluctuations. Although acoustic pressure amplification based on these criteria are predicted, they did not show the existence of self-sustaining or acoustically unstable results. The first study of self-sustaining thermoacoustic instabilities was presented by Zambon and Chelliah [78] for methane and air flames in 2006. In this study, they investigate the general acoustic pressure field determined by the geometry, and as such, do not impose any external perturbations as in the previous studies. Under the assumption of fully reflecting boundary conditions, they show the existence of self-sustaining thermoacoustic oscillations. At higher strain rates, the amplification of thermoacoustic instabilities is much larger. They also show that the implementation of a single-step reaction exhibits much larger amplification than a detailed chemical kinetic model. A dual counterflowing premixed flame is also studied, and the acoustic amplification of the premixed flame is shown to be much larger than the diffusion flame. This work is interesting as it demonstrates many of the previous predictions of researchers, and at the same time, demonstrates that the waves in a counterflow diffusion flame can be self-sustaining. The work in this thesis aims to expand upon these results by studying the thermoacoustic response of a counterflow diffusion flame with a different fuel, namely, hydrogen. It is predicted that the larger density gradient between the low density hydrogen and the air may play a role in the thermoacoustic characteristics of the flame. In a slightly different configuration, Balasubramanian and Sujith [3] conducted a study on ducted diffusion flames under the assumption of infinite rate chemistry and found that the transient acoustic growth of these systems was on the order of $10^5$ to $10^7$, which would be extremely large. However, a correction by Magri and Juniper [2, 41] showed that, in fact, the transient growth was on the order of 1 to 10 for these ducted diffusion flames. As such, the actual growth of these acoustic perturbations is more modest than thought. A new study by Zhou *et al.* [80] showed that the response of a non-premixed flame to acoustic excitations are dependent on the resonance of the burner geometry.

# Chapter 3

# Mathematical Formulation

## 3.1 Governing Equations

### 3.1.1 Steady Counterflow Diffusion Flames

Analytically and numerically, the appeal of the round jet counterflow diffusion flame lies in its ability to be reduced to a quasi one-dimensional problem. The problem admits a self-similar solution, and through an analysis along the stagnation streamline, the partial differential equations can be expressed as a set of ordinary differential equations which depend on the axial direction only. To reduce the problem, two primary simplifying assumptions are made [31]:

- The velocity field can be described by a separable streamfunction $\Psi(x, r) = r^2 U(x)$, where $x$ is the axial direction, $r$ is the radial direction, and $U(x)$ is a function of $x$ only.
- Properties such as density, temperature, and species composition vary only in the axial direction.

The definition of the axisymmetric stream function is given by [31]:

$$\frac{\partial \Psi}{\partial r} = \rho u r = 2rU \tag{3.1}$$

$$-\frac{\partial \Psi}{\partial x} = \rho v r = -r^2 \frac{\mathrm{d}U}{\mathrm{d}x} \tag{3.2}$$

These relationships are rearranged for substitution into the Navier-Stokes equations. The resulting equations for the steady axisymmetric stagnation flow representing the counterflow diffusion flame are written as follows [31]:

$$\frac{\mathrm{d}\rho u}{\mathrm{d}x} + 2\rho V = 0 \tag{3.3}$$

$$\rho u \frac{\mathrm{d}V}{\mathrm{d}x} + \rho V^2 = -\Lambda + \frac{\mathrm{d}}{\mathrm{d}x}\left(\mu \frac{\mathrm{d}V}{\mathrm{d}x}\right) \tag{3.4}$$

$$\rho u \frac{\mathrm{d}u}{\mathrm{d}x} = -\frac{\mathrm{d}p}{\mathrm{d}x} + \frac{4}{3}\frac{\mathrm{d}}{\mathrm{d}x}\left[\mu \frac{\mathrm{d}u}{\mathrm{d}x} - \mu V\right] + 2\mu \frac{\mathrm{d}V}{\mathrm{d}x} \tag{3.5}$$

$$\rho c_p u \frac{\mathrm{d}T}{\mathrm{d}x} = \frac{\mathrm{d}}{\mathrm{d}x}\left(\lambda \frac{\mathrm{d}T}{\mathrm{d}x}\right) - \sum_{k=1}^{n} J_k \frac{\mathrm{d}h_k}{\mathrm{d}x} - \sum_{k=1}^{n} h_k \dot{\omega}_k \tag{3.6}$$

$$\rho u \frac{\mathrm{d}Y_k}{\mathrm{d}x} = -\frac{\mathrm{d}J_k}{\mathrm{d}x} + \dot{\omega}_k \tag{3.7}$$

where $u$ is the axial velocity, $\rho$ is the density, $\Lambda = (1/r)(\partial p/\partial r)$ is the pressure eigenvalue, $\lambda$ is the mixture thermal conductivity, $c_p$ is the mixture specific heat capacity, $\mu$ is the mixture dynamic viscosity, $p$ is the pressure, $h_k$ is the sensible enthalpy of species $k$, $\dot{\omega}_k$ is the mass production rate of species $k$, and $V = v/r$ is the scaled radial velocity. Note that the energy equation in this case includes only the thermal energy. The term $J_k = \rho Y_k V_k$ represents the diffusive flux of species $k$, where $Y_k$ is the species mass fraction and $V_k$ is the diffusion velocity. The formulation of $J_k$ depends on the diffusion model. Three primary diffusion models are typically used: the unity Lewis number model, which assumes that all molecular diffusivities are equal to the heat diffusivity; the mixture averaged model, which assumes binary diffusion between a species and an average mixture of the remaining components; and the multicomponent diffusion model, which solves the full mass diffusion matrix which includes the interactions between every species. Physically, the multicomponent model is deemed to be the most realistic; however, computationally, it is much more expensive. The cheapest method computationally is the unity Lewis number assumption [77]; however, it has been shown experimentally that in many cases the lighter species such as $H_2$ may experience preferential diffusion, and as such, have a higher diffusivity [7, 18, 40, 61]. The effects can alter the global flame structure and create other instabilties such as the diffusional-thermal instabilities which manifest themselves as a striped pattern in diffusion flames [35, 33]. The effects of the common diffusion modelling assumptions have been studied by many researchers, for example, Bruno *et al.* [10], who show that the mixture averaged model and the multicomponent model give comparable results. In this thesis, the

mixture averaged model is employed. The diffusion velocity is calculated as [31]:

$$V_k = -\frac{1}{X_k} D'_{km} \nabla X_k \tag{3.8}$$

where $X_k$ is the mole fraction of species $k$ and $D'_{km}$ is the diffusion coefficient between species $k$ and the remaining mixture. Note that the governing equations must be closed with an equation of state relating the pressure, temperature, and density of the mixture.

There are a number of codes which can solve the counterflow diffusion flame (many of them in-house). One of the most popular codes is Cantera [25], which solves the steady equations. Cantera is an open source software package which is used in solving problems regarding thermodynamics, chemical kinetics, transport properties, and laminar reacting flows. In this thesis, Cantera is used to obtain the steady one-dimensional flame solutions and to evaluate the thermophysical and transport properties. Note that in Equations 3.3-3.7, the axial momentum equation is decoupled from the other equations and is not necessary for determining the temperature, composition, or velocity fields [31]. As such, in the steady case, the axial momentum equation is only useful to obtain the axial pressure gradient. With the assumption that the pressure variations due to the pressure gradient are small relative to the mean thermodynamic pressure, Cantera calculates the solution to these equations under the isobaric assumption and does not solve the axial momentum equation.

### 3.1.2 Unsteady Counterflow Diffusion Flames

For the unsteady counterflow diffusion flame, we follow the formulation presented by Zambon and Chelliah [78]. In order to consider the unsteady effects and perturbations, we can expand any variable about $r = 0$. For any variable $\phi(x, r, t)$, the variable is expanded near the axis of symmetry ($x$ axis) as:

$$\phi(x, r, t) = \phi_0(x, t), \phi_1(x, t)r + \phi_2(x, t)r^2 + \dots \tag{3.9}$$

Due to symmetry, the first order term $\phi(x, t) \equiv 0$ except for the radial velocity, which is approximated as $v = V(x, t)r$ where $V$ is the first order term $v_1$, or in the previous section, the scaled radial velocity $V = v/r$.

The other variable which requires special attention is the pressure. The pressure is expanded as:

$$p(x,r,t) = p_0(x,r,t) + p_2(x,t) \tag{3.10}$$

During the formulation of the governing equations, we obtained a term for the pressure eigenvalue, $\Lambda = (1/r)(\partial p/\partial r)$. The pressure eigenvalue is dependent upon the strain rate of the problem, which is related to the nozzle separation distance and the inlet velocities. Under the isobaric assumption, the pressure term is expressed as [58, 78]:

$$p(x,r,t) = p_0 + \frac{1}{2}\Lambda r^2 \tag{3.11}$$

where $\Lambda = 2p_2$. Some studies have been conducted with $p_2$ or $\Lambda$ changing in time, which corresponds to a changing strain rate over time and a constant axial pressure [78]. However, to investigate the effects of thermoacoustic instabilities, we need to see how the axial pressure field changes with time. Consequently, in this study the pressure eigenvalue is held constant. Instead, the work is focused on the term $p_0$, which is decomposed into a constant mean and a fluctuating component:

$$p_0(x,r,t) = \overline{p}_0 + p_0'(x,t) \tag{3.12}$$

Here, $\overline{p}_0$ is the base pressure of the system, and $p_0'$ are the acoustic fluctuations from the base pressure. Note that $p_0$ is the thermodynamic pressure and can be calculated based on the other thermodynamic properties using an equation of state, for example, the ideal gas equation of state.

For the compressible unsteady solver, we would like to express Equations 3.3-3.7 in the conservative form. Additionally, the energy equation includes the kinetic energy as well, and the enthalpy is expressed in terms of the total enthalpy, $h_t = h + 1/2\,(u^2)$. In conservative form, the fluxes are expressed as $\frac{\mathrm{d}(\rho u)\phi}{\mathrm{d}x}$, where $\phi$ is the variable under consideration. From the streamfunction relations given in Equations 3.1 and 3.2, we have:

$$\rho u = 2U \tag{3.13}$$

$$\rho\frac{v}{r} = \rho V = -\frac{\mathrm{d}U}{\mathrm{d}x} \tag{3.14}$$

We use these relations to express the equations in conservative form. For example, for the axial momentum, $\phi = u$. The flux can be expanded by considering the chain rule:

$$\frac{\mathrm{d}\rho u u}{\mathrm{d}x} = \rho u\frac{\mathrm{d}u}{\mathrm{d}x} + u\frac{\mathbf{d}\rho u}{\mathrm{d}x} \tag{3.15}$$

Note that $\rho u = 2U$, then the second term on the right hand side becomes:

$$u\frac{\mathrm{d}\rho u}{\mathrm{d}x} = 2u\frac{\mathrm{d}U}{\mathrm{d}x} \tag{3.16}$$

Now, from Equation (3.14), the term becomes:

$$u\frac{\mathrm{d}\rho u}{\mathrm{d}x} = -2u\rho V \tag{3.17}$$

Then, we can replace the flux with its conservative form by:

$$\rho u\frac{\partial u}{\partial x} = \frac{\partial \rho u u}{\partial x} + 2u\rho V \tag{3.18}$$

This method is applied to all of the steady governing equations to obtain the equations in the conservative form. After conducting the necessary manipulations, the equations for the compressible axisymmetric laminar counterflow diffusion flame can be written in conservative form as follows [78]:

$$\frac{\partial \rho}{\partial t} + \frac{\partial \rho u}{\partial x} + 2\rho V = 0 \tag{3.19}$$

$$\frac{\partial \rho Y_k}{\partial t} + \frac{\partial \rho u Y_k}{\partial x} + \frac{\partial \rho V_k Y_k}{\partial x} + 2\rho Y_k V = \dot{\omega}_k \tag{3.20}$$

$$\frac{\partial \rho u}{\partial t} + \frac{\partial \rho u u}{\partial x} + \frac{\partial p_0}{\partial x} + 2\rho u V = \frac{\partial}{\partial x}\left[\frac{4}{3}\mu\left(\frac{\partial u}{\partial x} - V\right)\right] + 2\mu\frac{\partial V}{\partial x} \tag{3.21}$$

$$\frac{\partial \rho V}{\partial t} + \frac{\partial \rho u V}{\partial x} + 3\rho V^2 = -2p_2 + \frac{\partial}{\partial x}\left[\mu\frac{\partial V}{\partial x}\right] \tag{3.22}$$

$$\begin{aligned}\frac{\partial \rho h_t}{\partial t} - \frac{\partial p_0}{\partial t} + \frac{\partial \rho u h_t}{\partial x} + 2\rho h_t V = \frac{\partial}{\partial x}\left[\lambda\frac{\partial T}{\partial x}\right] - \sum_k \frac{\partial \rho Y_k V_k h_k}{\partial x} \\ + \frac{\partial}{\partial x}\left[\frac{4}{3}\mu\left(\frac{\partial u}{\partial x} - V\right)u\right] + 2\mu\frac{\partial V}{\partial x}u - \frac{4}{3}\mu\left(\frac{\partial u}{\partial x} - V\right)V\end{aligned} \tag{3.23}$$

The formulation here includes the axial momentum in the conservation of energy equation, resulting in the enthalpy being expressed as the total enthalpy $h_t = h + 0.5u^2$. Unlike in the steady case where the axial momentum equation was neglected, in the unsteady case we include the axial momentum equation in the solution to account for the effects of the unsteady pressure fluctuations. Note that the inclusion of the term $p_0$ in the axial momentum equation eliminates the need for the external forcing [78] typical of other studies.

### 3.1.3 Equation of State

The governing equations require closure through a relationship between various physical and thermodynamic properties, for example, the temperature, pressure, and density, through an equation of state (EoS). One of the most commonly applied equations of state is the ideal gas EoS:

$$p = \rho RT \tag{3.24}$$

where $R = R_u/W$, where $R_u$ is the universal gas constant and $W$ is the mixture molecular weight. The ideal gas assumption is typically valid at low pressures and densities. At high pressures, the ideal gas behaviour is also recovered at the high temperatures found within the flame region where the compressibility factor approaches unity [4]. As such, the applicability of the ideal gas assumptions must consider both the pressure and the temperature. The speed of sound $c$ for an ideal gas can be calculated as:

$$c = \sqrt{\gamma RT} \tag{3.25}$$

where $\gamma = c_p/c_v$ is the specific heat ratio and $R$ is the specific gas constant.

The present numerical code is developed with the ability to integrate more complex state equations such as the Peng-Robinson, Soave-Redlich-Kwong or any other EoS for the computation of high-pressure systems.

### 3.1.4 Chemical Kinetic Mechanisms

One of the difficulties in combustion simulations is the modelling of the chemical reactions. The simplest model of the chemical reaction process is a one-step, global, irreversible reaction. Typically, the overall global reaction can be written quite simply. For example, for a hydrogen and oxygen flame, the global reaction can be written as:

$$2H_2 + O_2 \longrightarrow 2H_2O \tag{3.26}$$

The reaction rate can be determined through an Arrhenius-type law. Although the global reaction can describe the overall conversion of reactants to products, this one-step global reaction has embedded in it some unphysical assumptions about the underlying combustion process. For the chemical reaction to progress, the molecules need to collide, dissociate, and then recombine to form the products. Physically, this cannot happen simultaneously and

this multi-step process is not reflected within the global reaction equation. In reality, there are a number of intermediate reactions which occur to produce intermediate species. The combustion process can be described by considering all of these intermediate reactions, and this collection of reactions is referred to as the combustion or chemical kinetic mechanism. Because the solution of the governing equations becomes very computationally expensive with the addition of more species (each species requiring its own transport equation), one active field of research is in identifying reduced combustion mechanisms. The goal is to create the simplest mechanism possible which accurately reproduces the combustion process. In this study, we employ the chemical kinetic mechanism for $H_2$-$O_2$ combustion developed by Burke *et al.* [11]. The mechanism contains 9 species and 27 reactions to describe the oxidation of $H_2$. This chemical mechanism is particularly well-suited for high-pressure hydrogen combustion.

### 3.1.5 Boundary Conditions

#### Steady State Simulation

The boundary conditions of the steady-state solutions obtained from Cantera are set based on the desired operating conditions of the system. At the inlets, the temperature, species mass fractions, and mass flow rates are prescribed. The scaled radial velocity $V$ is set to 0 at the bounds. For a domain from $x = 0$ to $x = L$, the boundary conditions are given as:

$$Y(0) = Y_0, \quad Y(L) = Y_L \tag{3.27}$$

$$T(0) = T_0, \quad T(L) = T_L \tag{3.28}$$

$$\rho(0)u(0) = \dot{m}_0, \quad \rho(L)u(L) = \dot{m}_L \tag{3.29}$$

$$V(0) = V(L) = 0 \tag{3.30}$$

The pressure is set to a constant base pressure throughout the domain in accordance with the isobaric assumption. Typically, the momentum of both inflows is balanced such that the stagnation plane lies in the center of the domain.

#### Unsteady Simulation

The boundary conditions for the unsteady solution are more complex because the treatment of the thermoacoustic oscillations and resultant waves must be considered. To account for

the reflection of the waves, we implement time-dependent boundary conditions, namely, the Navier-Stokes Characteristic Boundary Conditions (NSCBC) [51]. At a high level, the NSCBC aim to capture physically realistic reflections and transmissions of waves. First, the characteristic waves which are exiting the boundary from the interior are calculated. Then, this information can be used to calculate the characteristic waves which would be incoming into the domain from the exterior of the boundary to obtain the desired behaviour, for example, for fully reflecting waves. Finally, depending on the number of desired boundary conditions, a number of conservation equations at the boundary are replaced by inviscid boundary conditions which include the characteristic waves calculated previously. The equations are then advanced in time at the boundaries to obtain solutions for all of the variables in the system. At the left side inlet ($x = 0$), for an inflow boundary condition, we have one outgoing wave with amplitude $L_1$, and two corresponding incoming waves with amplitudes $L_2$ and $L_5$. The amplitude of the outgoing wave is obtained through calculations of the one-sided derivatives from the interior of the domain. The outgoing wave is calculated as [51]:

$$L_1 = (u - c)\left[\frac{\partial p_0}{\partial x} - \rho c \frac{\partial u}{\partial x}\right] \tag{3.31}$$

where $c$ is the local speed of sound. If perfect reflection of the acoustic waves is desired, the incoming waves are calculated as [51]:

$$L_2 = 0 \tag{3.32}$$
$$L_5 = -L_1 \tag{3.33}$$

Using these relationships, a new equation for the axial velocity at the bounds is introduced [78]:

$$\frac{\partial \rho u}{\partial t} + u\frac{1}{c^2}\left[L_2 + \frac{1}{2}(L_5 + L_1)\right] + \frac{1}{2c}[L_5 - L_1] = 0 \tag{3.34}$$

By integrating this equation, we obtain a new value for the updated axial inlet velocity, which we use as the target value when setting the ghost cells. The implementation of the ghost cells is discussed in a later section. If we want to have partially reflecting boundary conditions, we can calculate the incoming wave $L_5$ as [51, 78]:

$$L_5 = K(p_0 - \overline{p}_a) \tag{3.35}$$

where $K$ is a damping coefficient and $\overline{p}_a$ is the ambient pressure. The term $K$ is expressed as [51]:

$$K = \sigma \left(1 - M^2\right) \frac{c}{L} \tag{3.36}$$

where $\sigma$ is a constant, $M$ is the Mach number, and $L$ is the characteristic length of the flow domain. When $\sigma = 0$, the amplitude of the reflected waves is set to 0 and as such, results in perfectly non-reflecting boundary conditions. For more physical dampening of waves, $\sigma = 0.25$ is typically used [44]. In other cases, $\sigma$ can be varied to yield partially reflecting waves. Once $L_5$ is calculated, we require another equation to update the density or pressure at the inlet [78]:

$$\frac{\partial \rho}{\partial t} + \frac{1}{c^2}\left[L_2 + \frac{1}{2}\left(L_5 + L_1\right)\right] = 0 \tag{3.37}$$

After determining the correct $\rho$, the pressure $p_0$ can also be set through an equation of state relating the thermodynamic properties.

For the right side inlet ($x = L$), the calculation of the characteristic waves is slightly different from the left inlet, mainly due to the speed at which the wave is travelling. The outgoing wave is calculated as:

$$L_5 = (u + c)\left[\frac{\partial p_0}{\partial x} + \rho c \frac{\partial u}{\partial x}\right] \tag{3.38}$$

For perfect reflection, the incoming waves are:

$$L_2 = 0 \tag{3.39}$$

$$L_1 = -L_5 \tag{3.40}$$

For partial or no reflection, the incoming wave for $L_1$ is calculated as:

$$L_1 = K\left(p_0 - \overline{p}_a\right) \tag{3.41}$$

The equations which are integrated to advance the boundary conditions remain the same as for the left side inlet. The one-sided derivatives of the outgoing waves are calculated via the second order forward difference on the left:

$$\frac{\partial u}{\partial x} \approx \frac{-3u_i + 4u_{i+1} - u_{i+2}}{2\Delta x} \tag{3.42}$$

and the second order backward difference on the right:

$$\frac{\partial u}{\partial x} \approx \frac{3u_i - 4u_{i-1} + u_{i-2}}{2\Delta x} \tag{3.43}$$

### 3.1.6 Initial Conditions

#### Steady State Simulations

The steady state simulations are obtained using Cantera. The initial number of desired grid points is given as an input. Based on the stoichiometry, the values for the grid points are interpolated and then the solver is run to fit the solution to the governing equations. In some cases where convergence is difficult, the solution may first be attempted with the energy equation disabled (constant temperature profile). Once the solution is converged, the energy equation can be enabled to ensure the solution satisfies all of the governing equations.

Once the solution is fully converged, a grid refinement is conducted based on the user-defined tolerances. In this case, grid points are added or removed depending on the refinement criteria. It is typical to initialize the solution on a small number of points, for example, 7 points, and then have Cantera automatically refine the grid. Cantera has three refinement criteria and one pruning criterion. The tolerances are defined based on the ratio of grid spcing between points, the slope or fractional change of value between points, and the curvature or fractional change of derivative between points. Cantera will then automatically refine the grid and add points based on these criteria. Cantera can also remove unnecessary grid points in a pruning process, although this may be disabled if required. For situations where we require an over-resolved grid, it is important to disable the pruning.

#### Unsteady Simulations

The initial conditions for the unsteady solution is provided by a steady solution obtained through Cantera. Obtaining a solution from Cantera requires two main considerations. First, the grid resolution for capturing acoustics in the unsteady case is much more strict than in the steady case. Second, there is a requirement on the maximum grid spacing

between two points in the unsteady case. As such, we must obtain a heavily over-resolved steady state solution from Cantera to act as our initial conditions for the unsteady solution. For example, we may achieve a grid converged solution with only around 120 points from Cantera; however, such a grid does not satisfy the requirements for the unsteady case. As such, the initial solution from Cantera must be initialized with a much larger number of grid points, for example, 1000. This ensures that the final solution has a sufficient resolution for use in the unsteady case.

After the steady solution is obtained from Cantera, the resultant values are used to initialize the solution for the unsteady compressible solver. Because of the different discretization and solution schemes between the two solvers, this initialization strategy also serves the purpose of introducing some broadband pressure fluctuations into the system. If we set the boundary conditions to perfectly non-reflecting, these perturbations are allowed to pass through the boundaries and we can obtain a steady state solution using the new solver. If the boundary conditions are set to reflecting boundary conditions, then the characteristic waves are reflected at the boundary, either perfectly or partially. In this way, we may investigate the interaction between these reflected waves and the flame. In the case of self-sustaining acoustic waves, these reflected waves will be excited by the interactions with the flame and become self-sustaining without the need for any external input. In this case, we do not depend on an external pressure forcing term to study the amplification of the acoustic waves.

## 3.2 Numerical Method

### 3.2.1 Development of Code

The in-house Python code which has been developed for this project is a one-dimensional finite volume code which solves the unsteady conservative form of the axisymmetric stagnation flow equations presented in Section 3.1.2. The code is parallelized and interfaces with Cantera [25] to calculate the transport and thermodynamic properties. The time-dependent NSCBC have also been implemented into the code to allow for a detailed study of the acoustics.

#### Flux Reconstruction

To solve the governing equations, we require information about the fluxes at each cell wall. To calculate the fluxes at the cell walls, we adopt a fairly new approach known as the flux

reconstruction approach [28]. A schematic diagram of the technique is shown in Figure 3.1. Consider the 'true' solution to be the solid black line. However, we only have information at the markers. The question becomes, how do we obtain an approximate value for the 'true' solution in between the points, for example, at the dotted line? The flux reconstruction approach relies on a polynomial interpolation using variable stencils to compute the flux. The general approach is as follows:

1. The left-biased flux (red dotted line) is calculated using two points to the left of the dotted line and one point to the right.
2. The right-biased flux (blue dotted line) is calculated using two points to the right of the dotted line and one point to the left.
3. The left- and right-biased fluxes are averaged at the dotted line to obtain an approximation for the 'true' solution at that location.

To calculate the biased fluxes, a second order polynomial is fit through the appropriate points. The number of points required for interpolation is one more than the interpolation order. By selecting a second order polynomial, we obtain a code that is between second and third order accurate, although the exact accuracy is difficult to compute analytically.

The flux reconstruction approach has a number of benefits. First of all, the technique introduces some slight numerical dissipation into the code, which helps with the stability of the solution. Secondly, the stencil and polynomial order for the interpolations can be increased to increase the spatial resolution. A schematic diagram of the flux reconstruction approach in the context of the code is shown in Figure 3.2. On the computational side, the flux reconstruction is well-suited for parallelization. As this approach only requires a single ghost cell on each decomposed MPI block, only the flux at the internal boundary faces need to be communicated between neighboring MPI processes.

The flux reconstruction scheme necessitates some special considerations on the boundary conditions. Because we need information on either side of the cell faces, we add one ghost cell to either end of the domain to calculate the flux at the boundaries. For the boundary fluxes, the flux is interpolated from the inside of the domain only. The ghost cell values are set to obtain the correct behaviour at the boundary cell face, for example, to maintain a Dirichlet or Neumann boundary condition. The details of the boundary conditions are presented in Section 3.1.5. In most cases, the ghost cells are set for Dirichlet conditions based on the values obtained through the NSCBC; however, in other applications, Neumann or Robin boundary conditions could also be applied.

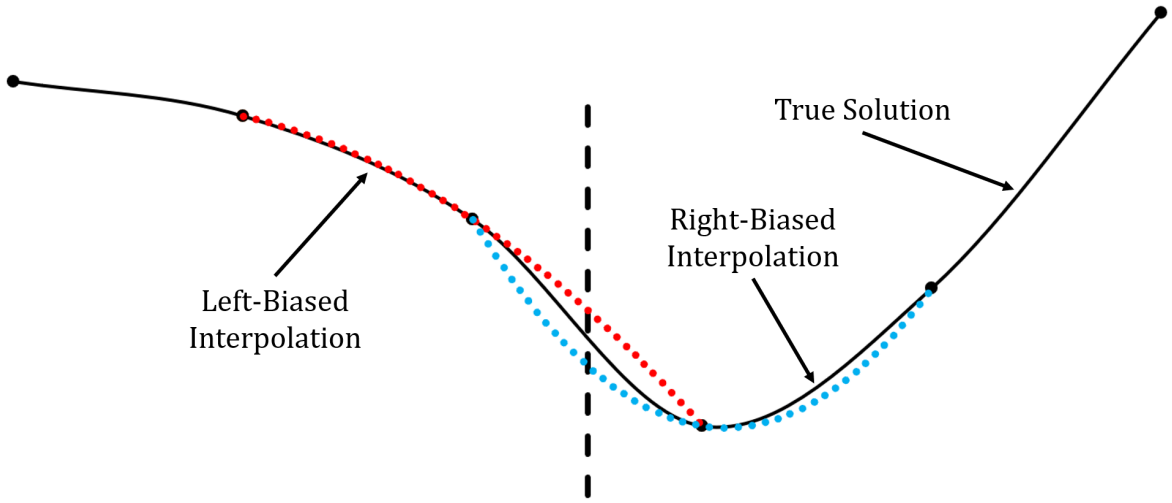


Figure 3.1: Schematic diagram of the flux reconstruction approach. The solid black line represents the 'true' solution, whereas the markers represent the available information.

For the solution of the governing equations, we can express the system of questions in vector form:

$$\frac{\partial \mathbf{Q}}{\partial t} + \frac{\partial \mathbf{F}}{\partial x} = \frac{\partial \mathbf{R}}{\partial x} + \mathbf{S} \tag{3.44}$$

where $\mathbf{Q}$ are the conserved variables, $\mathbf{F}$ are the convective fluxes, and $\mathbf{R}$ are the source terms. The vectors are:

$$\mathbf{Q} = \begin{pmatrix} \rho \\ \rho Y_k \\ \rho u \\ \rho V \\ \rho h_t - p_0 \end{pmatrix} \tag{3.45}$$

$$\mathbf{F} = \begin{pmatrix} \rho u \\ \rho u Y_k \\ \rho u u + p_0 \\ \rho u V \\ \rho u h_t \end{pmatrix} \tag{3.46}$$

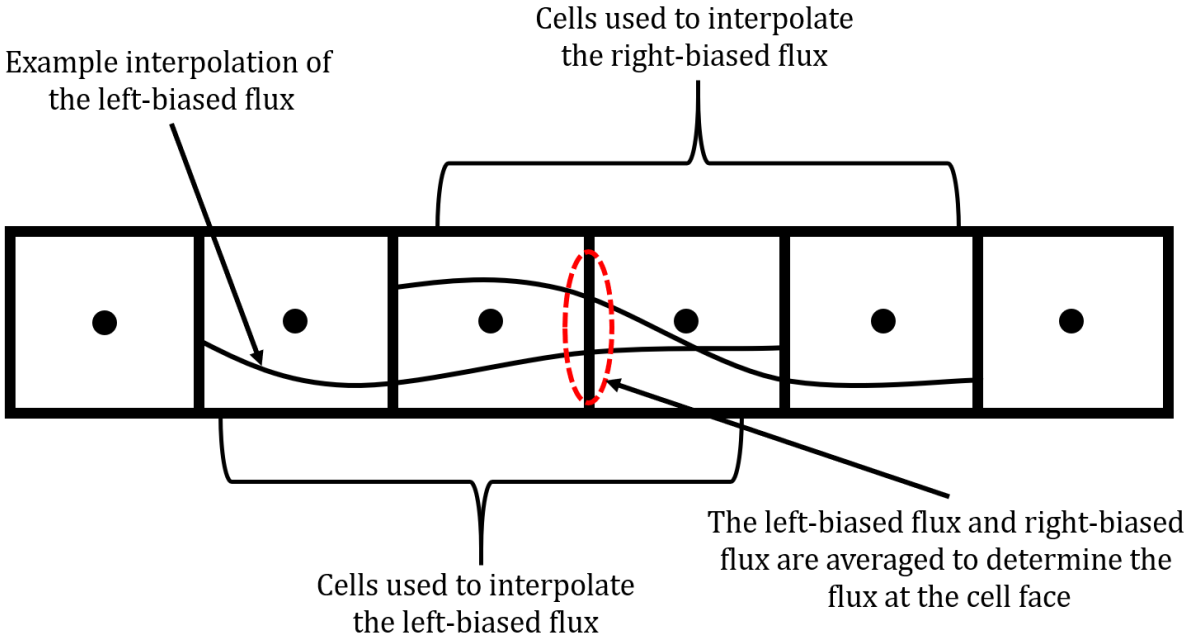


Figure 3.2: Schematic diagram of the flux reconstruction approach in the context of the code.

$$\mathbf{R} = \begin{pmatrix} 0 \\ -\rho u V_k Y_k \\ \frac{4}{3}\mu\left(\frac{\partial V}{\partial x} - V\right) \\ \mu\frac{\partial V}{\partial x} \\ \lambda\frac{\partial T}{\partial x} - \sum_k \rho Y_k V_k h_k + \frac{4}{3}\mu\left(\frac{\partial u}{\partial x} - V\right) u \end{pmatrix} \tag{3.47}$$

$$\mathbf{S} = \begin{pmatrix} -2\rho V \\ -2\rho Y_k V + \dot{\omega}_k \\ -2\rho u V + 2\mu\frac{\partial V}{\partial x} \\ -3\rho V^2 - 2p_2 \\ -2\rho h_t V + 2\mu\frac{\partial V}{\partial x}u - \frac{4}{3}\mu\left(\frac{\partial u}{\partial x} - V\right) V \end{pmatrix} \tag{3.48}$$

In the solution of the equations, the vectors $\mathbf{F}$ and $\mathbf{R}$ are first calculated with a left and right bias for either cell face, then the derivatives are approximated by differencing across the cell, consistent with the finite volume method. Then, the source terms are calculated and added to the solution.

Since the variables are solved in conservative form, we require special treatment to extract the primitive variables from the conservative variables. This is trivial for most variables, for example, to obtain $u$ we can simply calculate $u = \rho u/\rho$. The difficult variable is obtaining the temperature and pressure from the energy equation. The equations are solved for $\rho h_t - p_0$, and thus, a Newton solver is required to back out the appropriate temperature and pressure. If we assign a new variable $A = \rho h_t - p_0$ to be the calculated conservative flux, then we have to approximate the temperature and pressure such that the right hand side satisfies the calculated $A$. In the case of an ideal gas, the variables are first manipulated as:

$$\begin{aligned} A &= \rho h_t - p_0 && (3.49)\\ A &= \rho(h + 0.5u^2) - p_0 && (3.50)\\ A/\rho &= h + 0.5u^2 - p_0/\rho && (3.51)\\ A/\rho - 0.5u^2 &= h - RT && (3.52) \end{aligned}$$

Since all the terms on the left hand side are fully known through the solution of the governing equations, we set $F_{exact} = A/\rho - 0.5u^2$ and define a new function for the Newton solver:

$$G = F_{exact} - h + RT \tag{3.53}$$

We can then take the derivative with respect to $T$:

$$G' = -c_p + R \tag{3.54}$$

and the new temperature is approximated as:

$$T_{new} = T_{old} - G/G' \tag{3.55}$$

The new estimated $F_{est}$ is calculated as $F_{est} = h - RT$ and the pressure is calculated via the equation of state $p = \rho RT$. The process is iterated until $F_{exact}$ and $F_{est}$ are converged, providing the final values of $T$ and $p_0$. Note that a solver can also be implemented by exploiting the relationship between enthalpy ($h$) and internal energy ($e$):

$$e = h - \frac{p}{\rho} \tag{3.56}$$

in which case $F_{est} = e$, $G = F_{exact} - e$, and $G' = c_v$.

#### Time Discretization

The time stepping is conducted based on a fourth order Runge-Kutta method. Although the code can calculate the time stepping using a higher order Runge-Kutta method, the fourth order is sufficient for resolution of the acoustic pressure fluctuations. The prescribed CFL number is used to determine the maximum time step. The time step is calculated from the minimum grid spacing and the maximum velocity. The time step must also be sufficiently small such that the acoustic waves can be fully captured, with smaller time steps required for higher frequency fluctuations. Additionally, the implementation of the NSCBC also provides some limitations on the maximum CFL number due to numerical stability considerations.

### 3.2.2 Integration with Cantera

Although the in-house code is used to solve the governing equations, we also rely on Cantera [25] to calculate the thermophysical and transport properties, and the chemical source terms. Specifically, Cantera is used to calculate the mixture-averaged diffusion coefficients, chemical production rate ($\dot{\omega}_k$), enthalpy, viscosity, and thermal conductivity.

# Chapter 4

# Results

In this chapter, we present the results of various unsteady simulations of the counterflow diffusion flame. The results are obtained for a counterflow diffusion flame consisting hydrogen as the fuel and a mixture of oxygen and nitrogen as the oxidizer. Besides the varying strain rate, different boundary conditions are also tested to study the thermoacoustic behaviour of the counterflow diffusion flame.

## 4.1 Low Strain Rate

The first simulation is that of a low strain rate counterflow diffusion flame. The fuel is hydrogen, $H_2$ and the oxidizer is a mixture of nitrogen and oxygen, $0.7N_2/0.3O_2$ by mole fraction. The global strain rate is set to $a = 300$ s$^{-1}$ and the inlet separation distance is $L = 0.02$ m. These values correspond to fuel and oxidizer inlet velocities of $u_f = 4.75$ m/s and $u_o = -1.25$ m/s respectively. The fuel and oxidizer temperatures are $T_f = 295$ K and $T_o = 295$ K, and the overall pressure is 1 bar, or $1 \times 10^5$ Pa.

### 4.1.1 Steady Solution

The results are first obtained for the steady state solution with Cantera. The solution is then used as the initial conditions for the unsteady solver. The velocity profile of the flame in physical space is shown in Figure 4.1. The temperature and density profiles of the same flame are shown in Figure 4.2. The main reactant and product species profiles are presented in Figure 4.3 based on the mass fraction $Y$.

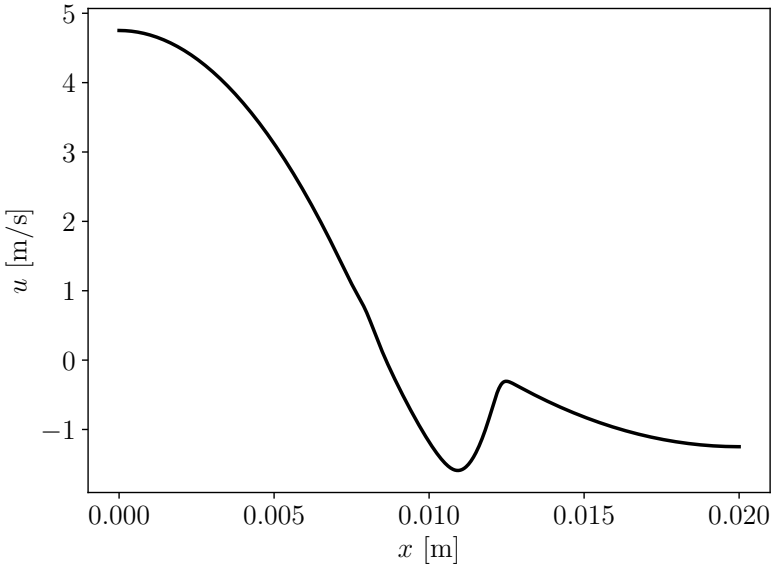


Figure 4.1: Velocity profile of the counterflow diffusion flame at a strain rate of $a = 300$ $s^{-1}$.

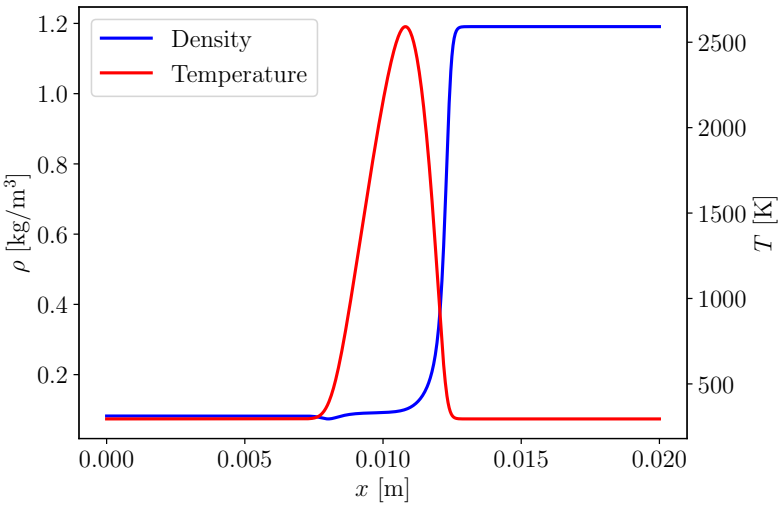


Figure 4.2: Temperature and density profiles of the counterflow diffusion flame at a strain rate of $a = 300$ $s^{-1}$.

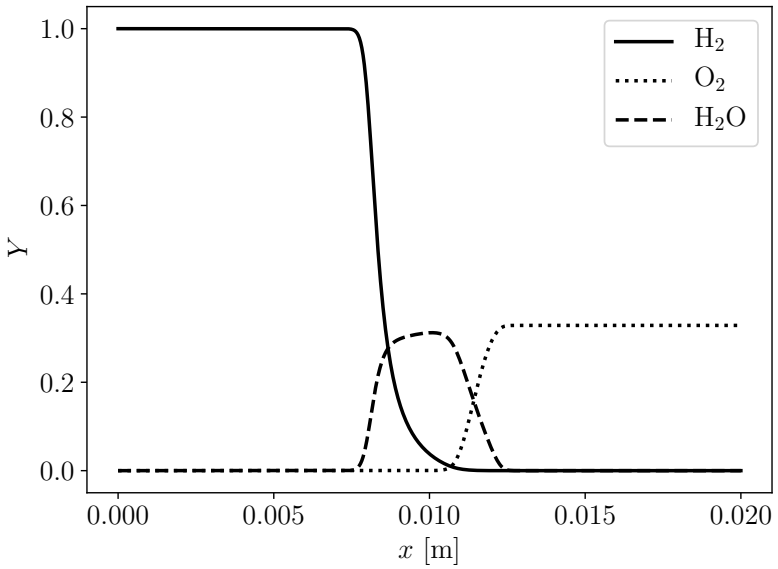


Figure 4.3: Major species profiles of the counterflow diffusion flame at a strain rate of $a = 300$ s$^{-1}$.

Besides the various profiles, the flame can also be characterised by its characteristic flame width, $\delta_f$. Following the method applied by Ribert *et al.* [55] in their study of the structure of counterflow diffusion flames, the flame width can be calculated by considering the full width of the flame at half of the maximum temperature. For the low strain rate flame at $a = 300$ s$^{-1}$, the flame width is calculated as $\delta_f = 0.0028$ m.

### 4.1.2 Validation

To validate our results, the steady state solution obtained from the new unsteady code is compared to the steady solution obtained from Cantera. The velocity, temperature, density, and radial velocity profiles are shown in Figure 4.4, and have very good agreement. In both cases, the solution is calculated on a uniform grid containing 1000 points, which results in a grid spacing of $\Delta x = 2 \times 10^{-5}$ m. Compared to the flame width $\delta_f = 0.0028$ m, our solution contains 140 points across the flame. For reference, Beardsell and Blanquart [5] had 20 points per flame thickness in their study of pressure fluctuations in premixed flames. Although the solver has requirements on the grid spacing overall, it is also important to ensure we have sufficient resolution in regions of high gradient, for example, the large density gradient near the center of the domain.

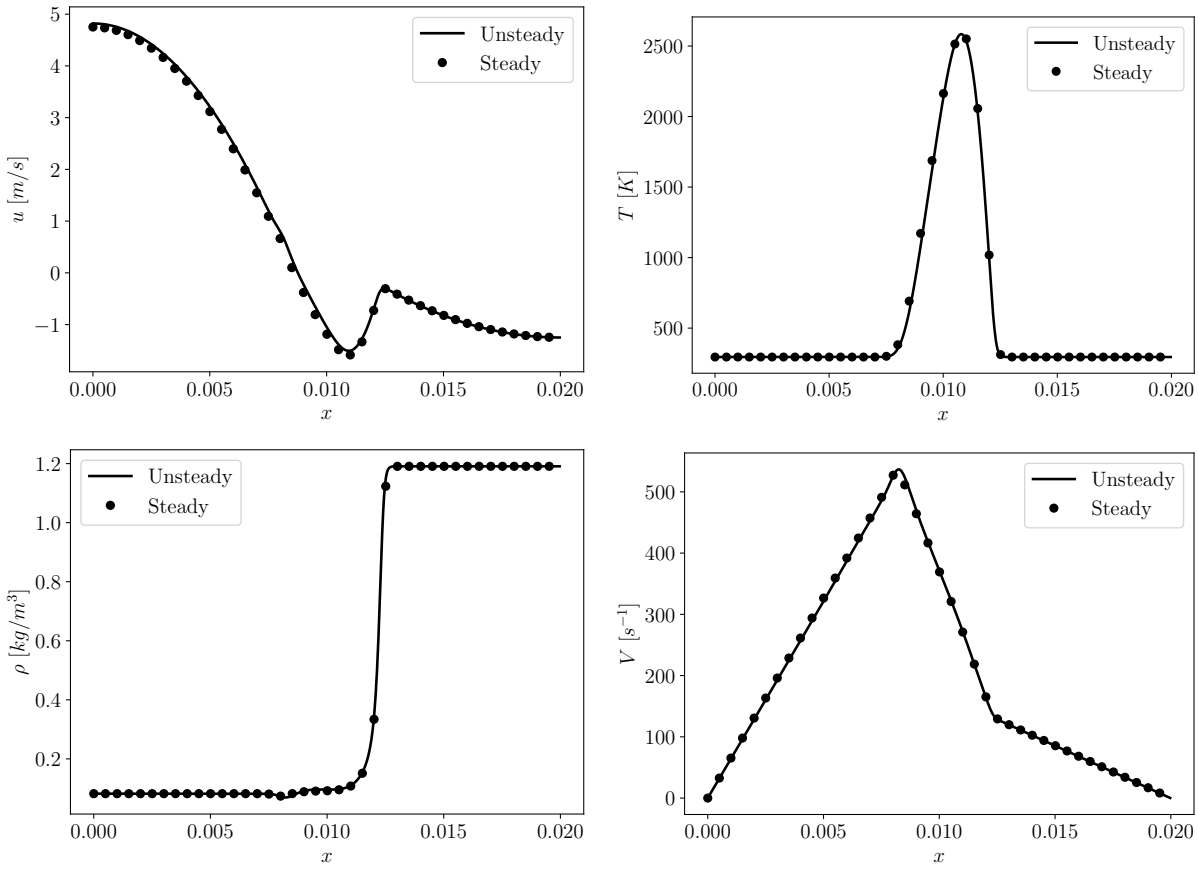


Figure 4.4: Comparison of the steady state solution obtained from our new code (line) with the steady solution obtained from Cantera (symbols).

### 4.1.3 Unsteady Solution

Because the steady solver and the unsteady solver have differing discretization and solution techniques, some acoustic pressure fluctuations are introduced into the solution as it adjusts to the fully compressible equations. The initial pressure perturbations are of fairly small amplitude, about 5-10 Pa, as shown in Figure 4.5. These initial perturbations are comparable to the initial perturbations of about 2-5 Pa reported by Zambon and Chelliah in their study [78].

The propagation of the initial acoustic perturbations is dependent on the boundary conditions of the problem, as described in Section 3.1.5. The effectiveness of the imple-

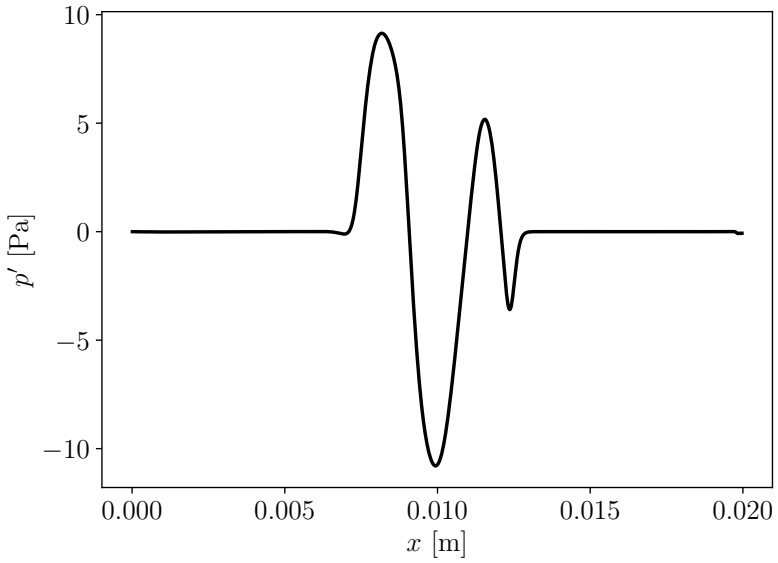


Figure 4.5: Initial acoustic pressure perturbations for the counterflow diffusion flame at a strain rate of $a = 300$ s$^{-1}$.

mented NSCBC is illustrated here. If the NSCBC are set to perfectly nonreflecting, the resultant damping of the acoustic waves can be seen in Figure 4.6, which shows the first reflection of the wave on either end of the domain. The reflections are significantly dampened after the first interaction of the waves with the boundaries. The remaining small perturbations exit the system after a number of additional interactions, finally resulting in the steady state pressure distribution shown in Figure 4.7. Note that the retention of the axial momentum equation in the solution of the governing equations produces a solution for the steady state pressure gradient, which is expected since the configuration is that of a stagnation flow. The underlying pressure gradient is small relative to the base pressure and the acoustic perturbations, and as such, a typical simplifying assumption is that of zero pressure gradient. In the lower strain rates with small axial velocities and under the low Mach number assumption, this approximation is justifiable [78]; however, the presence of the base pressure gradient may become more important at higher strain rates. In any case, the acoustic pressure perturbations can be extracted by subtracting the base underlying pressure field from the instantaneous pressure field.

The nonreflecting results can be compared to the fully reflecting case, presented in Figure 4.8. With these boundary conditions, the waves are not damped at all before reflection. The fully reflecting boundary conditions are the most favorable conditions for

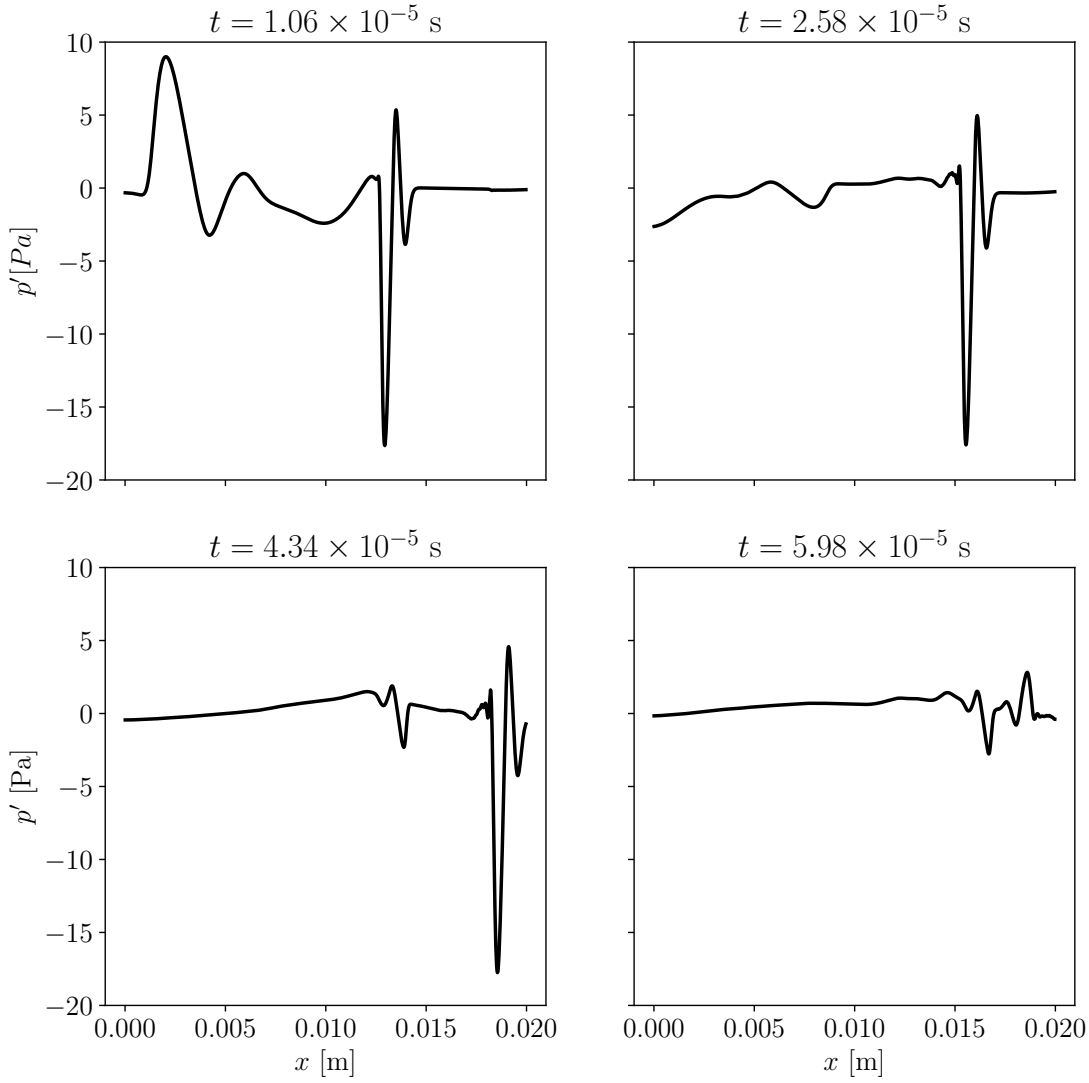


Figure 4.6: Damping of the initial acoustic pressure perturbations with nonreflecting boundary conditions for the counterflow diffusion flame at a strain rate of $a = 300$ s$^{-1}$.

thermoacoustic growth, as the amplitude of the wave is fully retained upon each reflection, and thus, any contribution from the flame to the pressure perturbations will be additive and fully retained as well.

What is particularly interesting about this study is the large disparity in the density of the propellants, and as such, the large gradient between the fuel and oxidizer densities.

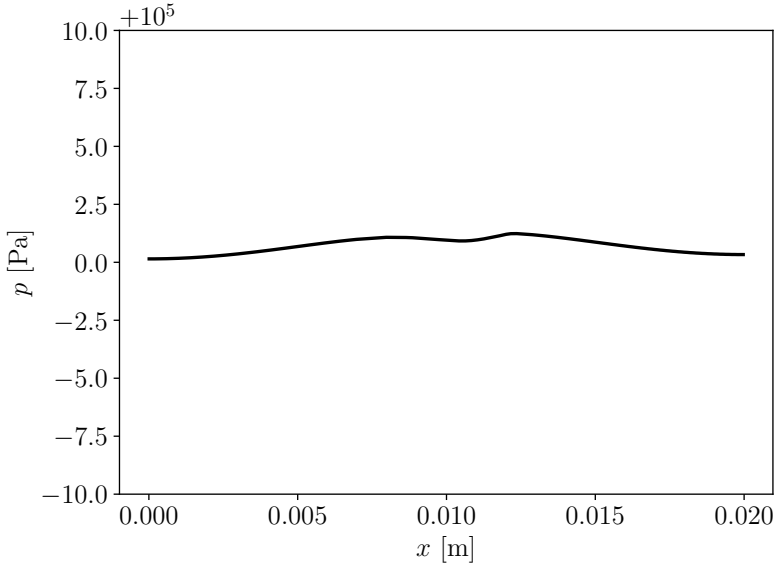


Figure 4.7: Steady state pressure field nonreflecting boundary conditions for the counter-flow diffusion flame at a strain rate of $a = 300\ \mathrm{s}^{-1}$.

The density in the fuel (hydrogen stream) is very low at $\rho_f = 0.082\ \mathrm{kg/m^3}$, and the density in the oxidizer (oxygen and nitrogen mixture) is much higher at $\rho_o = 1.19\ \mathrm{kg/m^3}$, which is about 14.5 times the fuel density. The difference in the density will necessarily impact the behaviour of the acoustic waves which travel through the system. As the waves hit the high density region from the low density region, part of the wave will be transmitted and part of the wave will be reflected. Additionally, the difference in the speed of sound between hydrogen and air is fairly large (around three times as fast), and as such, the waves coming from the low density side will have more interactions with the flame than those from the high density side. The previous study by Zambon and Chelliah [78] used methane and air as the reactants, which have much more similar densities and speeds of sound. The larger disparity between the acoustic properties of the fuel and oxidizer in our current study may yield some interesting phenomena in the thermoacoustics.

The growth of the acoustic perturbations was investigated by implementing the perfectly non-reflecting NSCBC. The pressure perturbations are extracted from two positions in the solution, one from the fuel stream (low density) and one from the oxidizer stream (high density). The axial locations are selected halfway between the inlets and the flame, and correspond to $x = 0.005$ m for the fuel stream and $x = 0.0015$ m for the oxidizer stream (see Figure 4.2). The results are shown in Figure 4.9. As can be seen, the initial

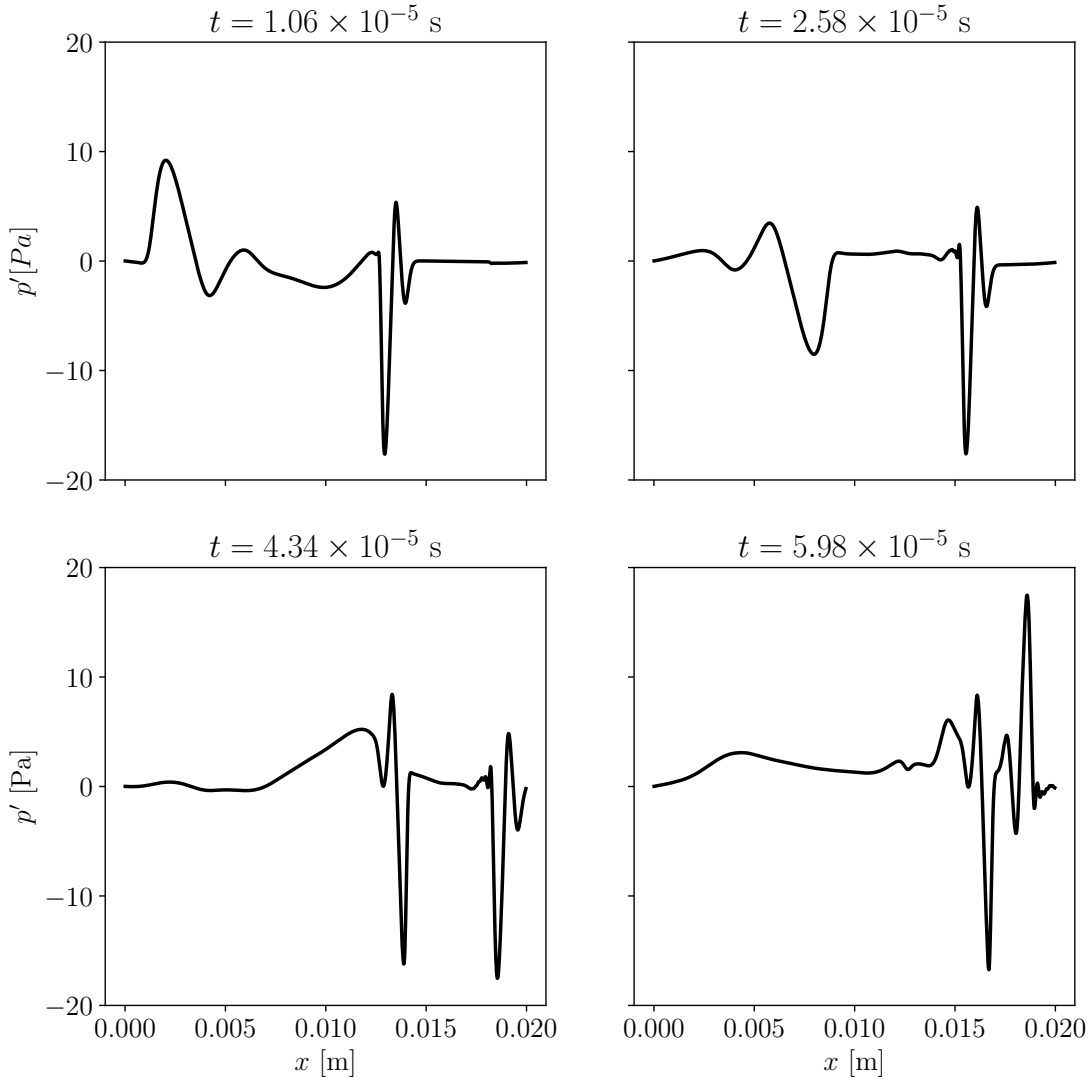


Figure 4.8: Reflection of the initial acoustic pressure perturbations with fully reflecting boundary conditions for the counterflow diffusion flame at a strain rate of $a = 300$ s$^{-1}$.

perturbations are around 5 Pa on the low density side and 10 Pa on the high density side. The results are captured for 10 ms. Considering that the speed of sound on the fuel stream is approximately $c_f = 1270$ m/s and the speed of sound on the oxidizer stream is approximately $c_o = 330$ m/s, this represents about 635 acoustic-flame interactions coming from the low density side and about 165 acoustic-flame interactions coming from the high

density side. Initially, the waves appear to be either consistent or slightly dampened until approximate $t = 0.004$ s, after which the acoustic perturbations are then amplified. The growth of the acoustic fluctuations in the low strain rate case is limited, growing from about 5 Pa to 15 Pa on the hydrogen side and 10 Pa to 20 Pa on the oxidizer side. This modest acoustic growth, with an amplification magnitude of 2-3 times the initial perturbations, is consistent with the results by Zambon and Chelliah [78] for counterflow diffusion flames and Magri *et al.* [41] for ducted diffusion flames. Note that Zambon and Chelliah [78] found that the growth of acoustic perturbations was present for non-premixed flames under the assumption of a one-step kinetic model; however, using a detailed model seemed to dampen the majority of the fluctuations. Their results also showed that the growth was much more significant at higher strain rates. Our current results show that with a different fuel (hydrogen instead of methane), even at a relatively low strain rate with a detailed kinetic model, we can also identify growth of the acoustic fluctuations with similar amplification magnitudes.

The dominant frequencies of these pressure fluctuations can be obtained through a spectral density analysis. This can be done through a number of ways, for example, through a Fourier periodogram. Since the timestep is not necessarily uniform for each step, we have unevenly spaced data. To extract the underlying periodicity of the signal, we apply the Lomb-Scargle periodogram. The Lomb-Scargle periodogram is a method of least-squares spectral analysis for unevenly spaced data first studied in detail by Lomb in 1975 [39] and further expanded by Scargle in 1982 [57]. The general procedure is that a spectrum of sinusoids are least-squared fit to the sampled data points. Consider a timeseries $X_j$ sampled at $t_j$ times for $N_t$ timesteps for $j = \{1, 2, \ldots, N_t\}$. If $X_j$ is scaled such that the mean is 0 and the variance is 1, the Lomb-Scargle periodogram is expressed as [57, 72]:

$$P(\omega) = \frac{1}{2}\left\{\frac{\left[\sum_j X_j \cos\omega\left(t_j-\tau\right)\right]^2}{\sum_j \cos^2\omega\left(t_j-\tau\right)} + \frac{\left[\sum_j X_j \sin\omega\left(t_j-\tau\right)\right]^2}{\sum_j \sin^2\omega\left(t_j-\tau\right)}\right\} \tag{4.1}$$

where $\tau$ is the frequency dependent time delay:

$$\tan 2\omega\tau = \frac{\sum_j \sin 2\omega t_j}{\sum_j \cos 2\omega t_j} \tag{4.2}$$

The periodogram is calculated for a range of trial frequencies to identify the peak frequencies.

The normalized Lomb-Scargle periodograms for the $a = 300$ s$^{-1}$ are shown in Figure 4.10. On the low density side, there are two distinct peaks at around 29 kHz and

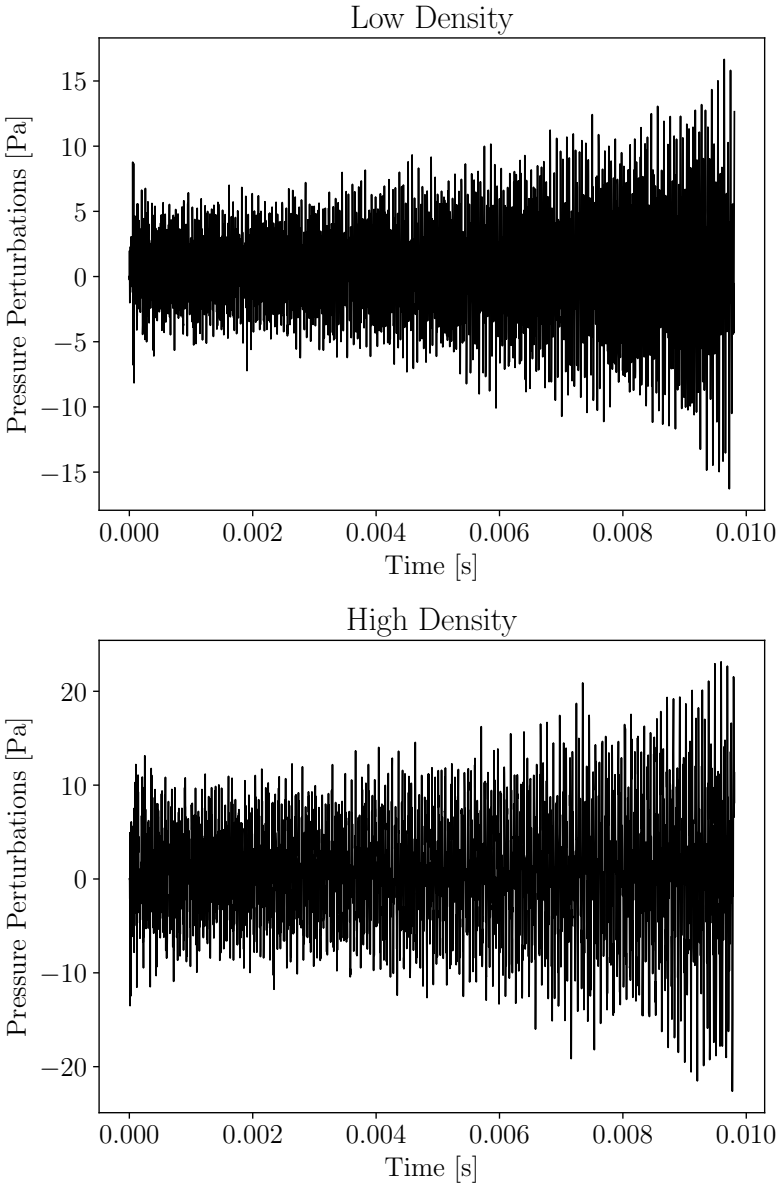


Figure 4.9: Growth of the acoustic perturbation of the low strain rate flame at $x = 0.005$ m (top) and $x = 0.015$ m (bottom).

77.5 kHz, with a smaller peak around 19 kHz. On the high density side, there is a distinct peak at 19 kHz, with secondary peaks at around 29 kHz and 77.5 kHz. The three

dominant peaks overlap between the low density and the high density side. The results are similar as those reported by Zambon and Chelliah [78], who found that the dominant half-wave mode frequency for a methane and air counterflow diffusion flame was around 19.5 kHz. However, it is important to note that the comparison of strain rate effects is not straightforward as the different fuels may respond differently to the same strain rates.

## 4.2 High Strain Rate

A high strain rate case is also computed, with the same operating conditions as the low strain rate with the exception of the inlet velocities. The higher strain rate is $a = 5000$ $s^{-1}$, corresponding to fuel and oxidizer inlet velocities of $u_f = 79.2$ m/s and $u_o = -20.8$ m/s respectively.

### 4.2.1 Steady Solution

The temperature and density profiles of the higher strain rate flame compared to the lower strain rate flame are shown in Figure 4.11. As expected, the higher strain rate flame is much thinner, having a flame thickness of about $\delta_f = 0.00074$ m, which is about 27% of the thickness of the lower strain rate flame. This simulation was conducted on a grid of 1074 points, which represents approximately 40 points per the flame thickness, which is still sufficient for resolution. Additionally, the maximum flame temperature is lower and the flame is shifted slightly to the left.

The counterflow diffusion flame is often represented in terms of the mixture fraction space as opposed to physical space, especially when discussing the flame structure. The flames in mixture fraction space are presented in Figure 4.12. Although the flame position is shifted in physical space, the flame is located at the same mixture fraction with a lower flame temperature. Additionally, the density profiles have some minor variations between the two, but this could be attributed to a slightly different different distribution of species (products and reactants) due to the different strain rates and the species diffusion.

### 4.2.2 Unsteady Solution

#### Perfectly Reflecting Boundary Conditions

For the unsteady results, the nonreflecting NSCBC have a similar behaviour as the lower strain rate, with the acoustic waves being heavily damped out to reveal an underlying base

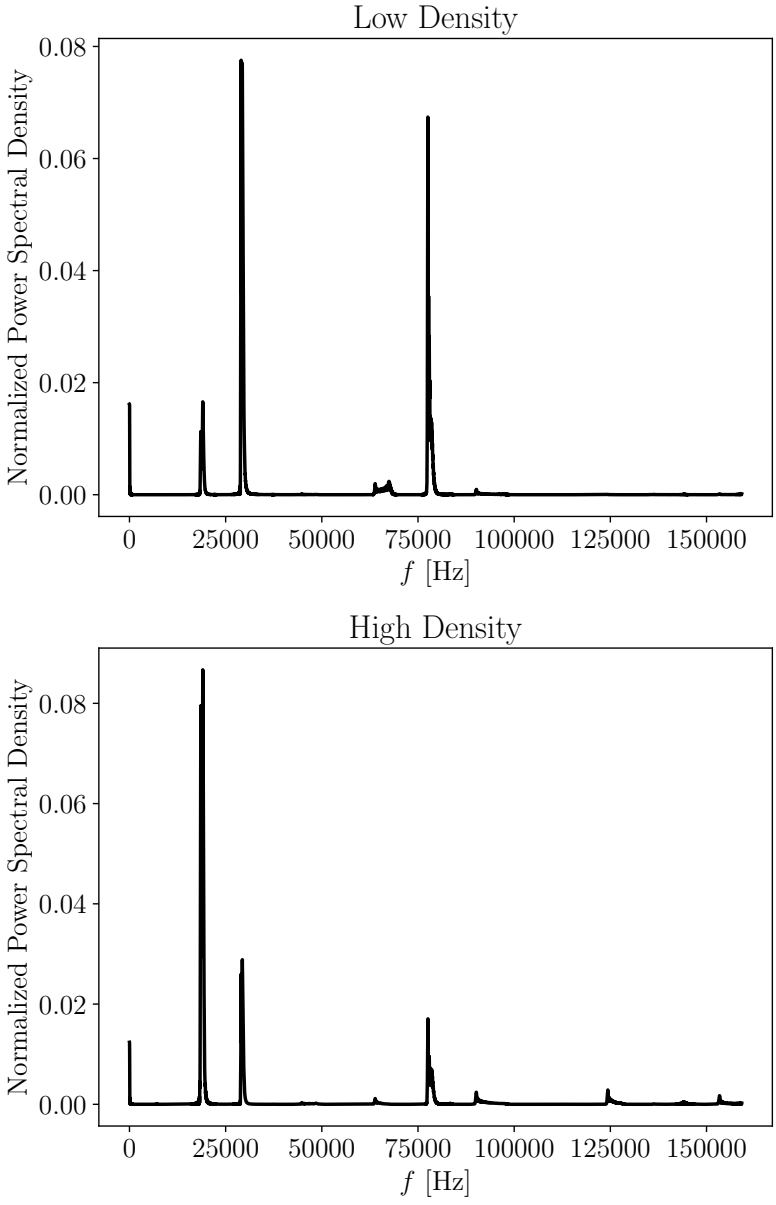


Figure 4.10: Normalised Lomb-Scargle periodograms for the low strain rate case of $a = 300$ $s^{-1}$.

pressure gradient. The initial perturbations for the high strain rate case are larger and approximately 60-80 Pa in amplitude.

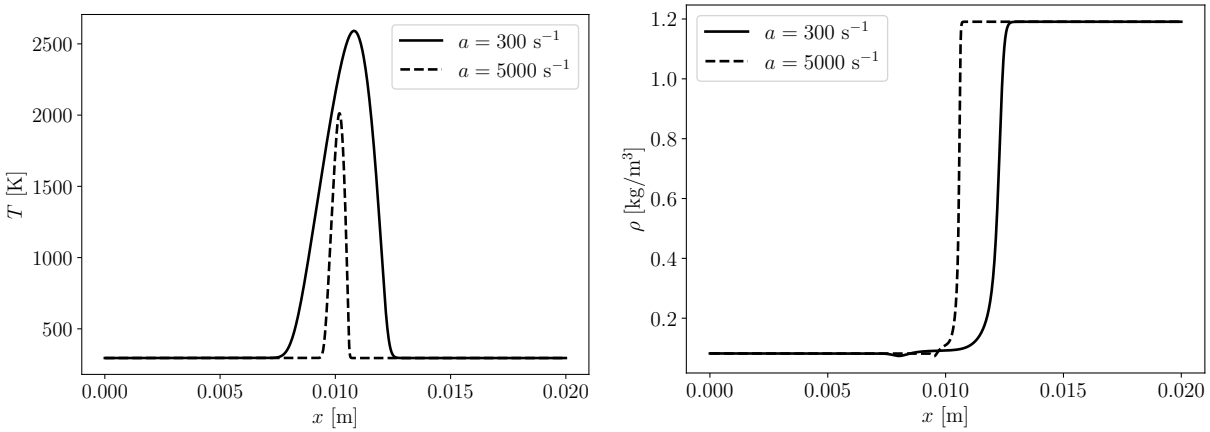


Figure 4.11: Temperature and density profiles of the counterflow diffusion flames in physical space.

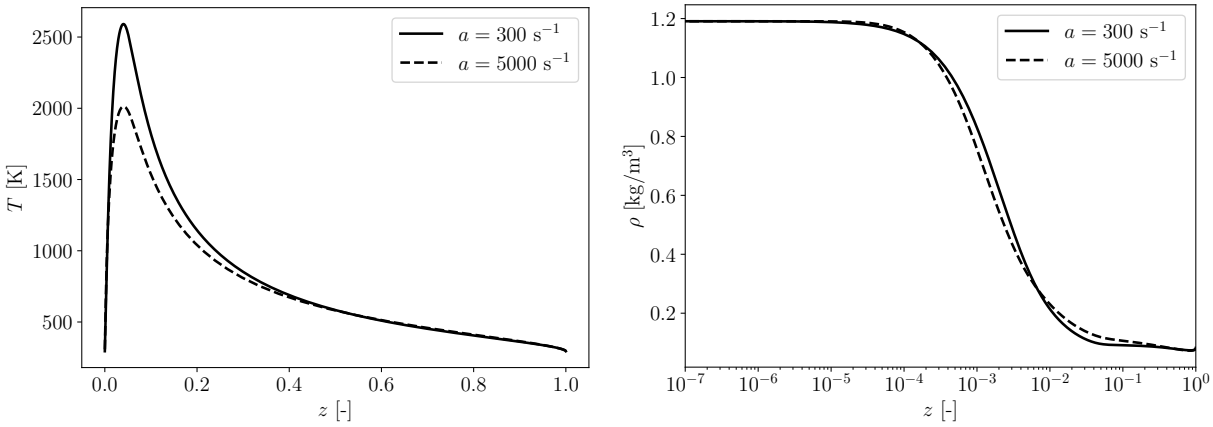


Figure 4.12: Temperature and density profiles of the counterflow diffusion flames in mixture fraction space.

The transient acoustic growth is presented in Figure 4.13. Compared to the low strain rate case, the acoustic growth is much more significant, reaching around 6000-8000 Pa for the peak amplitude for the tested time period. The growth also occurs across a much shorter timespan and has an amplification magnitude of about 100 times the size of the initial perturbations. Previous results have shown that counterflow diffusion flames near the extinction strain rate (highest strain rate before extinction) experience the most appreciable amplification of acoustic perturbations [64, 65]. The larger magnification of the acoustic

pressure perturbations for a higher strain rate is also reported by Zambon and Chelliah [78], although the difference is not as drastic. This can be attributed to the different reactants used, and also the larger difference between the strain rates in our case.

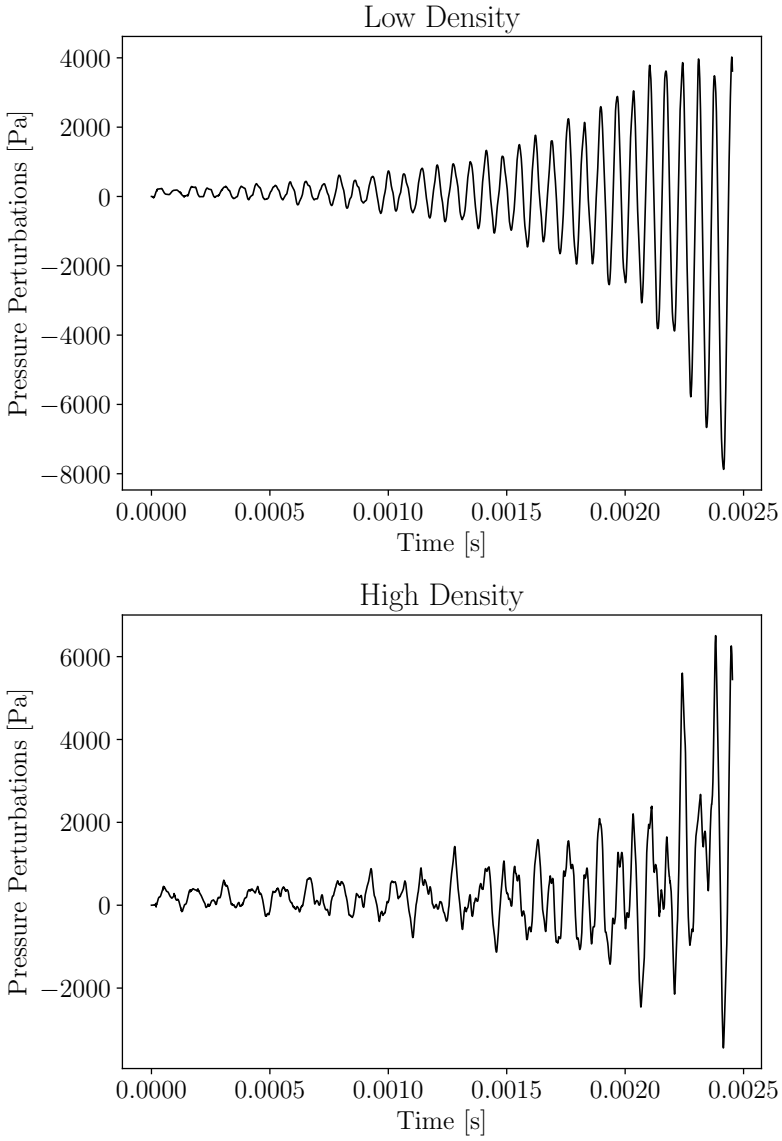


Figure 4.13: Growth of the acoustic perturbations of the high strain rate flame at $x = 0.005$ m (top) and $x = 0.015$ m (bottom).

Notably, the acoustic pressure perturbations in the high strain rate case have a much more distinct periodicity compared to the low strain rate case, especially in the low density (hydrogen) stream. The results of the spectral analysis are shown in Figure 4.14 for both propellant streams. In the hydrogen stream, the periodogram shows a distinct peak at around 14.5 kHz. In the oxidizer stream, the periodogram shows distinct peaks around 8 kHz, 14.5 kHz, and 19.7 kHz. The most dominant peaks overlap between both streams. Very small peaks at 8 kHz and 19.7 kHz can also be seen in the low density stream; however, they are very small compared to the dominant frequency peak. Although the dominant peak frequencies are different, the peak around 19 kHz exists in the high density stream for both the low and high strain rate cases. The periodogram was also calculated via the Fourier transform and showed the same dominant frequencies as the Lomb-Scargle periodograms.

Under the fully reflecting boundary conditions, the boundaries are set as pressure nodes for the system. Underlying the growth of the acoustic perturbations is the existence of standing wave behaviour, which is shown for both the pressure and velocity fluctuation fields shown in Figures 4.15 and 4.16. Although there are also smaller waves travelling across the flame, this underlying standing wave represents the fundamental mode. Similar results were reported for the methane and air counterflow diffusion flame by Zambon and Chelliah [78]; however, they had found the presence of one pressure antinode in the center of the computational domain. In our case, we find the existence of two antinodes. The first one is at approximately $x = 0.01$ m, which is where the very large density gradient is (see Figure 4.11). The second one is at approximately $x = 0.0175$ m within the higher density nitrogen-oxygen mixture. The corresponding velocity antinodes for the pressure nodes can be seen in Figure 4.16.

The acoustic perturbation growth for the pressure antinodes identified in Figure 4.15 are shown in Figure 4.17. The results are consistent with the underlying standing wave behaviour, as they both exhibit the same frequency and peak amplitudes. The profile selected at $x = 0.015$ m shown in Figure 4.13 is close to the pressure node identified in Figure 4.15, and as such, the fluctuations are dampened compared to the profile at $x = 0.0175$ m.

The corresponding Lomb-Scargle periodograms are shown in Figure 4.18. At $x = 0.01$ m, the peak frequency is at approximately 8.3 kHz, and at $x = 0.0175$ m, the peak frequency is at approximately 14.5 kHz. The periodogram of the left pressure antinode shows stronger peaks representing the harmonics of system, whereas the right pressure antinode has a much larger peak for the dominant frequency. Compared to the periodoggrams in Figure 4.14, the dominant frequencies are the same, although the appearance of the harmonics appears more clearly on the opposite side. As can be seen, the high strain rate case can be highly resonant

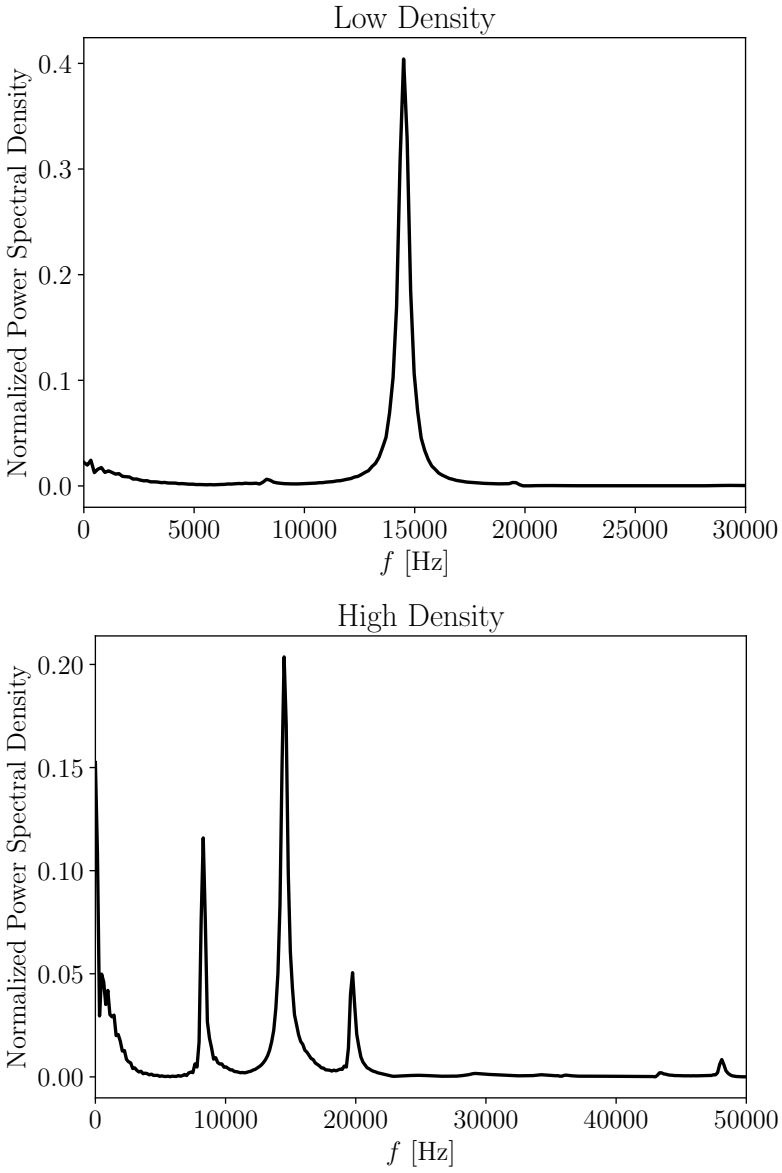


Figure 4.14: Normalized Lomb-Scargle periodograms for the high strain rate case of $a = 5000\ \mathrm{s}^{-1}$.

under the correct boundary conditions, and the natural frequencies can be extracted via a spectral analysis.

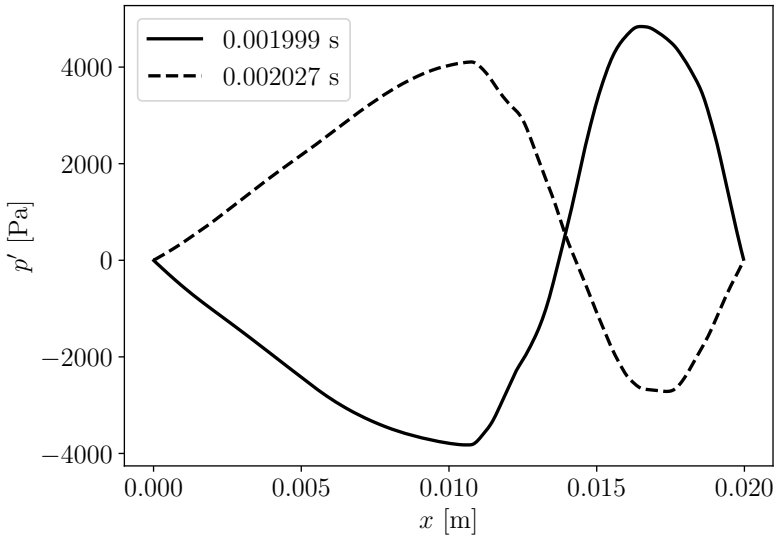


Figure 4.15: Two instantaneous snaphots of the pressure fluctuation field showing the underlying standing wave behaviour for $a = 5000$ s$^{-1}$.

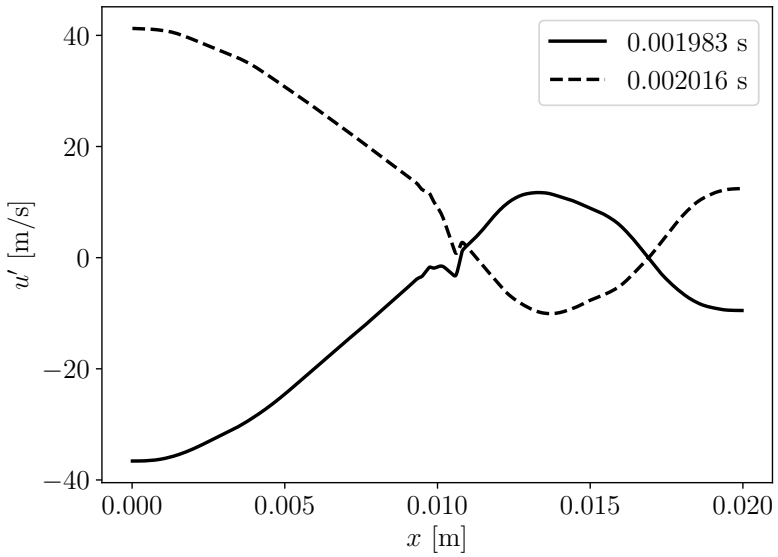


Figure 4.16: Two instantaneous snaphots of the velocity fluctuation field showing the underlying standing wave behaviour for $a = 5000$ s$^{-1}$.

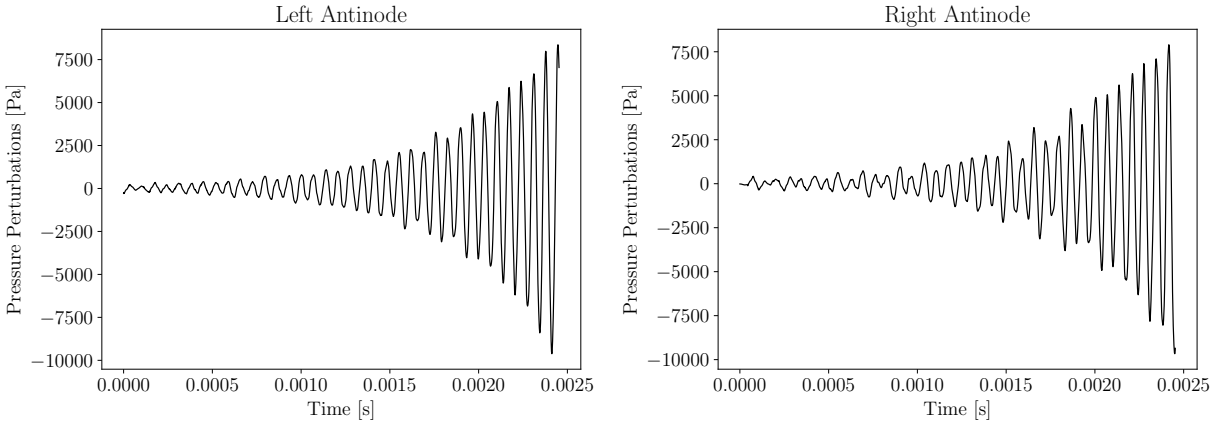


Figure 4.17: Growth of acoustic pressure perturbations at $x = 0.01$ m and $x = 0.0175$ m, corresponding to the locations of the antinodes of the underlying standing wave behaviour for the $a = 5000$ s$^{-1}$ case.

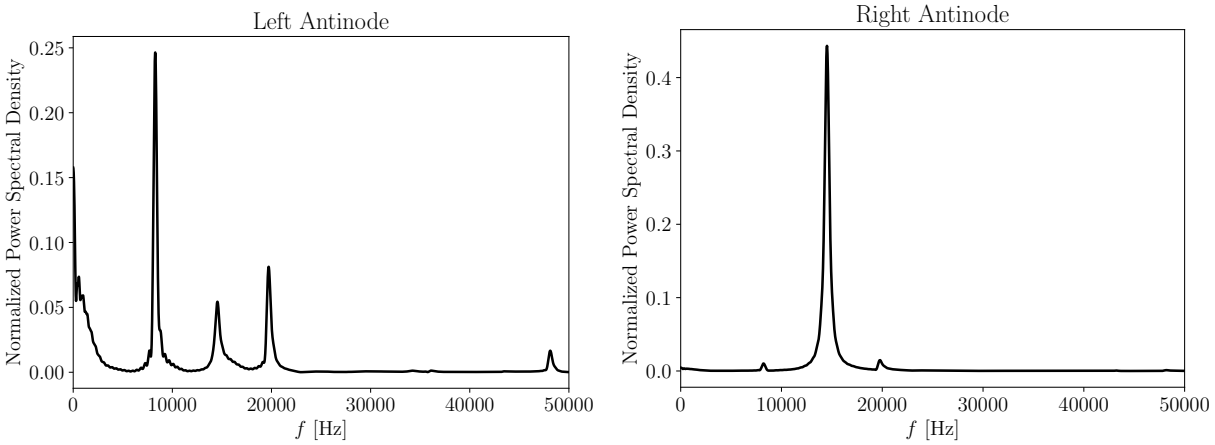


Figure 4.18: Normalized Lomb-Scargle periodograms at the pressure antinodes for the high strain rate case of $a = 5000$ s$^{-1}$.

A similar overall standing wave type behaviour can also be observed in the low strain rate case; however, the effects of smaller travelling waves are much more prominent, and the representation of the acoustic perturbation field is not as clear as it is for the high strain rate case.

### Partially Reflecting Boundary Conditions

In Section 3.1.5, we had also introduced the notion of partially reflecting boundary conditions. Because the perfectly or fully reflecting boundary conditions are the most optimal for the growth of the thermoacoustic fluctuations, it is also of interest to study whether the growth of these waves is sustainable even under the assumption of non-perfectly reflecting boundary conditions. As noted in Section 3.1.5, in the calculation of the characteristic wave amplitudes, the damped wave is introduced into the domain through the NSCBC (either $L_1$ or $L_5$ depending on which end of domain is being studied) as:

$$L = K(p_0 - \overline{p}_a) \tag{4.3}$$

where $K$ is a damping factor. The results calculated under a damping factor of $K = 1 \times 10^6$ are presented in Figure 4.19. As can be seen, despite these boundary conditions permitting only partial reflection of the acoustic waves, the acoustic waves are in fact sustained and even undergo some very minor growth. The peak amplitudes in both the low and high density streams have an amplification magnitude of approximately 2.

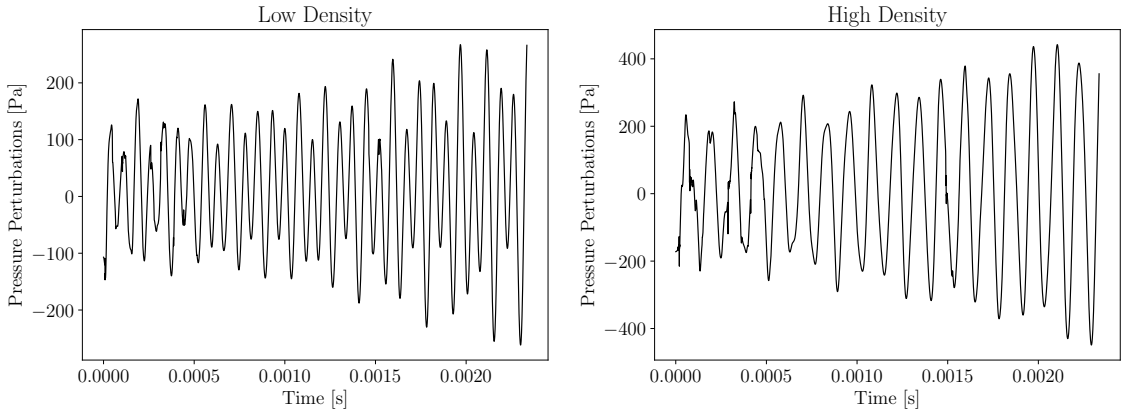


Figure 4.19: Growth of the acoustic perturbations of the high strain rate flame at $x = 0.005$ m (top) and $x = 0.015$ m (bottom) under partially reflecting boundary conditions with $K = 1 \times 10^6$.

To extract the frequencies of the fluctuations, the corresponding Lomb-Scargle periodograms are presented in Figure 4.20. In the low density stream the peak frequency is approximately 13.5 kHz, and in the high density stream the peak frequency is approximately 7.8 kHz. The frequencies are quite similar compared to the dominant frequencies presented in Figure 4.14.

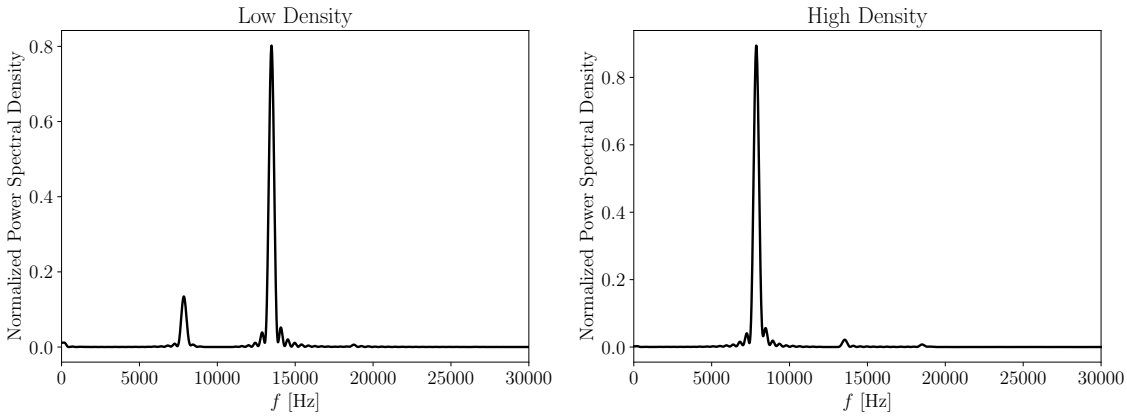


Figure 4.20: Normalized Lomb-Scargle periodograms for the high strain rate case of $a = 5000\ \mathrm{s}^{-1}$ under partially reflecting boundary conditions with $K = 1 \times 10^6$.

## 4.3 Thermoacoustic Response Under External Forcing

As discussed in the introduction, typically the thermoacoustic response of a flame is determined based on the Rayleigh criterion, such that the acoustic fluctuations are amplified or dampened based on the phase difference between the pressure and heat release fluctuations. For a counterflow diffusion flame, the amplification factor $H$ related to the Rayleigh criterion can be calculated as [65]:

$$H = \frac{1}{\tau} \int_0^\tau \frac{Q - Q_m}{Q_m} \sin(2\pi f t) \mathrm{d}t \tag{4.4}$$

where $\tau = 1/f$ is the period of oscillation. Typically, the integral is calculated over the whole period of an oscillation [45]. The heat release is integrated across the computational domain as [5]:

$$Q = \int_{x=0}^{x=L} \rho c_p \dot{\omega}_T \mathrm{d}x \tag{4.5}$$

where $\dot{\omega}_T$ represents the temperature production term, which can be calculated based on the species production rate as:

$$\dot{\omega}_T = -\frac{1}{c_p}\sum_{k=1}^{n} h_k \dot{\omega}_k \tag{4.6}$$

which is similar to the energy equation source term for the steady state governing equations.

To study the effects of acoustic amplification, we introduce a sinusoidal pressure wave from the fuel inlet:

$$p(t) = p_m + p_a \sin(2\pi f t) \tag{4.7}$$

where $p_a = 5000$ Pa, similar to the simulations conducted by Beardsell and Blanquart [5]. A number of different frequency oscillations (between 10-77.5 kHz) are introduced to evaluate the amplification factor. The results are presented in Table 4.1. For the majority of the frequencies in the low strain rate case the amplification factor is negative, which indicates that the acoustic oscillations are dampened. However, at $f = 10$ kHz, the acoustic amplification factor is positive, which indicates that the acoustic oscillations are excited. On the other hand, for the high strain rate case, the amplification factor is positive at the frequency $f = 77.5$ kHz, and larger than the low strain rate for the frequency $f = 10$ kHz.

Table 4.1: Acoustic amplification factor $H$ for various frequencies of forced pressure oscillations.

| Strain Rate $a$ [$s^{-1}$] | Frequency $f$ [kHz] | Amplification Factor $H$ |
|---|---|---|
| 300 | 10.0 | 0.0259 |
| 300 | 15.0 | -0.0306 |
| 300 | 19.5 | -0.0486 |
| 300 | 29.0 | -0.0301 |
| 300 | 77.5 | -0.0430 |
| 5000 | 10.0 | 0.0657 |
| 5000 | 77.5 | 0.0128 |

The results are consistent with the analysis of the acoustic growth presented earlier, which showed that the acoustic oscillations grow at a much higher rate for the high strain rate case compared to the low strain rate case. In the evaluation of the acoustic amplification factor, we find that a wider range of frequencies can yield a negative amplification factor for the low strain rate case compared to the high strain rate case, indicating that a wider range of fluctuations should be dampened in the low strain rate case. With regards to our current results, for the low strain rate case (see Figure 4.9), it can be seen that up

until $t \approx 0.004$ s, the acoustic perturbations do not grow in size, and may even be slightly dampened. Using a detailed kinetic model at a low strain rate for a methane and air flame, Zambon and Chelliah [78] showed that the initial acoustic perturbations would decay (see Figure 6 in their work). However, for our high strain rate case, the growth is immediate and the fluctuations become large within within 0.0025 s (see Figure 4.13). Additionally, because the higher strain rate flame amplifies a wider range of frequencies, the pressure oscillations may not completely decay even in the presence of partially reflecting boundary condition (see Figure 4.19). The evaluation of Rayleigh's criterion helps to explain some of the differences in the behaviour of our two strain rates.

# Chapter 5

# Conclusions and Future Work

## 5.1 Extension to Transcritical Combustion

In the current work, the behaviour of thermoacoustic fluctuations in the ideal gas counterflow diffusion flame were studied. Recent studies have shown the existence of high frequency thermoacoustic instabilities in high pressure liquid rocket engines [1], in which case the propellants may be transcritical. As such, it will be of interest to extend this work to consider transcritical fluids and supercritical fluids as well. When a fluid is transcritical, it is at a pressure above the critical pressure, but at a temperature below the critical temperature. Although there is no discrete phase change at supercritical pressures as there is for subcritical pressures, as the fluid increases in temperature and crosses the Widom line (the extension of the coexistence line), the fluid can undergo a rapid change from a high density liquid-like state to a low density gas-like state in a process referred to as pseudoboiling. The pseudoboiling process has two important and interesting characteristics. First of all, the density undergoes a drastic decrease, which can affect the dynamics of the system. Secondly, the specific heat capacity is characterized by a sharp peak at the pseudoboiling point. For example, in a LOX-GH2 combustor, the oxygen will be injected at transcritial conditions and thus undergo pseudoboiling. Figure 5.1 shows the drastic changes in density and specific heat capacity of oxygen at $p = 70$ bar as the fluid experiences a finite temperature difference. The interesting aspect of the transcritical combustion is the presence of the large density gradient across the pseudoboiling point. The interaction with the density gradient at the pseudoboiling point may have an effect on the behaviour of the thermoacoustic fluctuations.

To account for these real-fluid effects, we can close the governing equations with a cubic

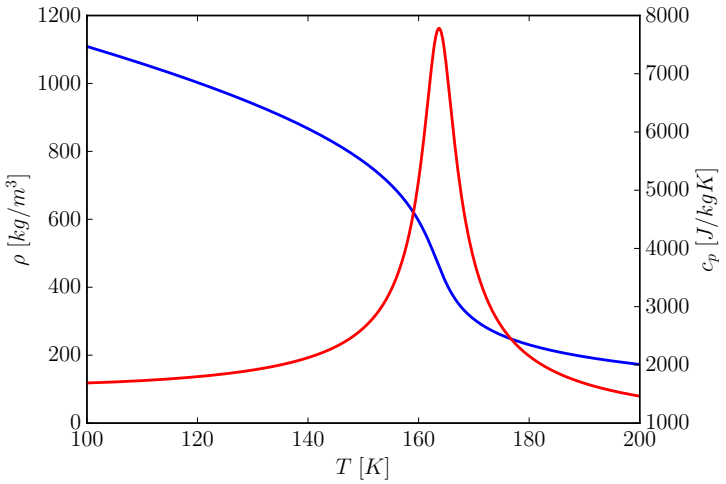


Figure 5.1: Density (blue) and specific heat capacity (red) of oxygen as it crosses the Widom line undergoing pseudoboiling at $p = 70$ bar. Values obtained from CoolProp [6].

EoS relating pressure, density, and temperature. One of the most commonly used is the Peng-Robinson EoS [48], which is given as:

$$P = \frac{RT}{V - b} - \frac{a\alpha}{V^2 + 2bV - b^2} \tag{5.1}$$

where:

$$\begin{aligned} a &= 0.45724\frac{R^2T_c^2}{P_c} \\ b &= 0.07780\frac{RT_c}{P_c} \\ \alpha &= \left(1 + \kappa\left(1 - \sqrt{T_r}\right)\right)^2 \\ \kappa &= 0.37464 + 1.54226\omega - 0.2699\omega^2 \end{aligned}$$

and $V$ is the molar volume. The subscripts $c$ and $r$ refer to the critical and reduced thermodynamic quantities respectively. For mixtures, mixing rules must be applied to calculate the critical properties and the subsequent EoS parameters. These parameters can be calculated via the classical mixing rules [54, 42]:

$$a\alpha = \sum_i^n \sum_j^n z_i z_j a_{ij} \alpha_{ij} \qquad b = \sum_i^n z_i b_i \tag{5.2}$$

The required mixture critical properties are calculated by:

$$T_{c,ij} = \left(T_{c,i} T_{c,j}\right)^{0.5} \left(1 - k_{ij}\right) \qquad V_{c,ij} = \left(\frac{V_{c,i}^{1/3} + V_{c,j}^{1/3}}{2}\right)^3 \qquad P_{c,ij} = \frac{Z_{c,ij} R T_{c,ij}}{V_{c,ij}} \tag{5.3}$$

$$Z_{c,ij} = 0.5\left(Z_{c,i} + Z_{c,j}\right) \qquad \omega_{ij} = 0.5\left(\omega_i + \omega_j\right)$$

where $k_{ij}$ are the binary interaction parameters typically determined experimentally. In many cases where there is insufficient experimental data, they are assumed to be zero. The departure from ideal gas thermodynamic properties, for example the specific heat capacity, must also be calculated.

## 5.2 Conclusions

In this work a code was developed to study the behaviour of self-sustaining thermoascoutic oscillations in the ideal gas hydrogen and oxygen/nitrogen counterflow diffusion flame. Two strain rates were studied, a low strain rate of $a = 300$ s$^{-1}$ and a high strain of $a = 5000$ s$^{-1}$. Under the assumption of perfectly reflecting boundary conditions, both cases were shown to self-sustain acoustic perturbations. However, the growth in the low strain rate case was minimal (on the order of 1-2 times as large across 0.01 s), whereas the growth of the high strain rate case was more significant in a much shorter period of time (on the order of 100 times as large across 0.0025 s). Since the growth was much more significant in the high strain rate case, the thermoacoustics were also studied under the assumption of partially reflecting boundary conditions. Although the boundaries are acoustically lossy, we find that the acoustic pressure perturbations can still be self-sustained. For all cases, the oscillations are decomposed using the Lomb-Scargle periodogram to identify the dominant frequencies. Additionally, a standing wave behaviour was identified from looking at instantaneous pressure profiles. To understand the behaviour better, various different frequency oscillations were introduced into the domain from the fuel inlet and the response was measured according to Rayleigh's criterion. For the low strain rate case, a variety of higher frequency oscillations were shown to be decaying but the lower frequency was shown to amplify, whereas for the high strain rate case, the higher and lower frequencies were both

amplified. The result is consistent with the findings of larger acoustic growth in the high strain rate case. The goal is to extend this work and conduct studies in the transcritical regime, where the unique thermodynamics near the critical point may play a larger role in the behaviour of the acoustic waves. The transcritical combustion is highly relevant to high pressure applications such as liquid rocket engines, and as such, such a study may help to shed some light on recent discoveries of intrinsic thermoacoustic instabilities in liquid rocket engines.

# References


[1] Wolfgang Armbruster, Justin S Hardi, Dmitry Suslov, and Michael Oschwald. Experimental investigation of self-excited combustion instabilities with injection coupling in a cryogenic rocket combustor. *Acta Astronautica*, 151:655–667, 2018.

[2] K Balasubramanian and RI Sujith. Non-normality and nonlinearity in combustion–acoustic interaction in diffusion flames–corrigendum. *Journal of Fluid Mechanics*, 733:680–680, 2013.

[3] Koushik Balasubramanian and RI Sujith. Non-normality and nonlinearity in combustion–acoustic interaction in diffusion flames. *Journal of Fluid Mechanics*, 594:29–57, 2008.

[4] Daniel T Banuti, Peter C Ma, Jean-Pierre Hickey, and Matthias Ihme. Thermodynamic structure of supercritical LOX–GH2 diffusion flames. *Combustion and Flame*, 196:364–376, 2018.

[5] Guillaume Beardsell and Guillaume Blanquart. Impact of pressure fluctuations on the dynamics of laminar premixed flames. *Proceedings of the Combustion Institute*, 37(2):1895–1902, 2019.

[6] Ian H. Bell, Jorrit Wronski, Sylvain Quoilin, and Vincent Lemort. Pure and pseudo-pure fluid thermophysical property evaluation and the open-source thermophysical property library coolprop. *Industrial & Engineering Chemistry Research*, 53(6):2498–2508, 2014.

[7] V Bergmann, W Meier, D Wolff, and W Stricker. Application of spontaneous raman and rayleigh scattering and 2D LIF for the characterization of a turbulent CH4/H2/N2 jet diffusion flame. *Applied Physics B*, 66(4):489–502, 1998.

[8] RW Bilger, SH Stårner, and RJ Kee. On reduced mechanisms for methane air combustion in nonpremixed flames. *Combustion and Flame*, 80(2):135–149, 1990.

[9] Sebastian Bomberg, Thomas Emmert, and Wolfgang Polifke. Thermal versus acoustic response of velocity sensitive premixed flames. *Proceedings of the Combustion Institute*, 35(3):3185–3192, 2015.

[10] Claudio Bruno, Vaidyanathan Sankaran, Hemanth Kolla, and Jacqueline H. Chen. Impact of multi-component diffusion in turbulent combustion using direct numerical simulations. *Combustion and Flame*, 162(11):4313–4330, 2015.

[11] Michael P. Burke, Marcos Chaos, Yiguang Ju, Frederick L. Dryer, and Stephen J. Klippenstein. Comprehensive H2/O2 Kinetic Model for High-Pressure Combustion. *International Journal of Chemical Kinetics*, 44(7):444–474, 2012.

[12] HK Chelliah, Chung King Law, T Ueda, MD Smooke, and FA Williams. An experimental and theoretical investigation of the dilution, pressure and flow-field effects on the extinction condition of methane-air-nitrogen diffusion flames. In *Symposium (International) on Combustion*, volume 23(1), pages 503–511. Elsevier, 1991.

[13] Emilien Courtine, Laurent Selle, and Thierry Poinsot. DNS of intrinsic thermoacoustic modes in laminar premixed flames. *Combustion and Flame*, 162(11):4331–4341, 2015.

[14] Alberto Cuoci, Alessio Frassoldati, Tiziano Faravelli, and ELISEO Ranzi. Frequency response of counter flow diffusion flames to strain rate harmonic oscillations. *Combustion Science and Technology*, 180(5):767–784, 2008.

[15] Alberto Cuoci, Alessio Frassoldati, Tiziano Faravelli, and ELISEO Ranzi. Formation of soot and nitrogen oxides in unsteady counterflow diffusion flames. *Combustion and Flame*, 156(10):2010–2022, 2009.

[16] N Darabiha. Transient behaviour of laminar counterflow hydrogen-air diffusion flames with complex chemistry. *Combustion science and technology*, 86(1-6):163–181, 1992.

[17] Michele E Decroix and William L Roberts. Study of transient effects on the extinction limits of an unsteady counterflow diffusion flame. *Combustion science and technology*, 146(1-6):57–84, 1999.

[18] MC Drake, M Lapp, CM Penney, S Warshaw, and BW Gerhold. Measurements of temperature and concentration fluctuations in turbulent diffusion flames using pulsed raman spectroscopy. In *Symposium (International) on Combustion*, volume 18(1), pages 1521–1531. Elsevier, 1981.

[19] Sébastien Ducruix, Daniel Durox, and Sébastien Candel. Theoretical and experimental determinations of the transfer function of a laminar premixed flame. *Proceedings of the combustion institute*, 28(1):765–773, 2000.

[20] FN Egolfopoulos. Geometric and radiation effects on steady and unsteady strained laminar flames. In *Symposium (International) on Combustion*, volume 25(1), pages 1375–1381. Elsevier, 1994.

[21] Fokion N Egolfopoulos. Structure and extinction of unsteady, counterflowing, strained, non-premixed flames. *International journal of energy research*, 24(11):989–1010, 2000.

[22] Fokion N Egolfopoulos and Charles S Campbell. Unsteady counterflowing strained diffusion flames: diffusion-limited frequency response. *Journal of Fluid Mechanics*, 318:1–29, 1996.

[23] T Emmert, S Bomberg, S Jaensch, and W Polifke. Acoustic and intrinsic thermoacoustic modes of a premixed combustor. *Proceedings of the Combustion Institute*, 36(3):3835–3842, 2017.

[24] Thomas Emmert, Sebastian Bomberg, and Wolfgang Polifke. Intrinsic thermoacoustic instability of premixed flames. *Combustion and Flame*, 162(1):75–85, 2015.

[25] Dave Goodwin, Harry K Moffat, and Raymond L Speth. Cantera: An object-oriented software toolkit for chemical kinetics, thermodynamics, and transport processes. *Caltech, Pasadena, CA*, 2009.

[26] Maarten Hoeijmakers, Viktor Kornilov, Ines Lopez Arteaga, Philip de Goey, and Henk Nijmeijer. Intrinsic instability of flame–acoustic coupling. *Combustion and Flame*, 161(11):2860–2867, 2014.

[27] Hongfa Huo, Xingjian Wang, and Vigor Yang. A general study of counterflow diffusion flames at subcritical and supercritical conditions: Oxygen/hydrogen mixtures. *Combustion and Flame*, 161(12):3040–3050, 2014.

[28] Hung T Huynh. A flux reconstruction approach to high-order schemes including discontinuous galerkin methods. In *18th AIAA Computational Fluid Dynamics Conference*, page 4079, 2007.

[29] HG Im, JK Bechtold, and Chung King Law. Counterflow diffusion flames with unsteady strain rates. *Combustion science and technology*, 106(4-6):345–361, 1995.

[30] Albert Jordà Juanós and William A Sirignano. Pressure effects on real-gas laminar counterflow. *Combustion and Flame*, 181:54–70, 2017.

[31] Robert J Kee, Michael E Coltrin, and Peter Glarborg. *Chemically reacting flow: theory and practice*. John Wiley & Sons, 2005.

[32] Jacob J Keller. Thermoacoustic oscillations in combustion chambers of gas turbines. *AIAA journal*, 33(12):2280–2287, 1995.

[33] JS Kim. Diffusional-thermal instability of diffusion flames in the premixed-flame regime. *Combustion science and technology*, 118(1-3):27–48, 1996.

[34] JS Kim and FA Williams. Contribution of strained diffusion flames to acoustic pressure response. *Combustion and Flame*, 98(3):279–299, 1994.

[35] JS Kim, FA Williams, and PD Ronney. Diffusional-thermal instability of diffusion flames. *Journal of Fluid mechanics*, 327:273–301, 1996.

[36] Taehoon Kim, Yongmo Kim, and Seong-Ku Kim. Numerical analysis of gaseous hydrogen/liquid oxygen flamelet at supercritical pressures. *International Journal of Hydrogen Energy*, 36(10):6303–6316, 2011.

[37] JS Kistler, CJ Sung, TG Kreut, Chung King Law, and M Nishioka. Extinction of counterflow diffusion flames under velocity oscillations. In *Symposium (International) on Combustion*, volume 26(1), pages 113–120. Elsevier, 1996.

[38] Guilhem Lacaze and Joseph C Oefelein. A non-premixed combustion model based on flame structure analysis at supercritical pressures. *Combustion and Flame*, 159(6):2087–2103, 2012.

[39] Nicholas R Lomb. Least-squares frequency analysis of unequally spaced data. *Astrophysics and space science*, 39(2):447–462, 1976.

[40] Marshall B Long, Sten H Stårner, and Robert W Bilger. Differential diffusion in jets using joint PLIF and Lorenz-Mie imaging. *Combustion science and technology*, 92(4-6):209–224, 1993.

[41] Luca Magri, K Balasubramanian, RI Sujith, and Matthew P Juniper. Non-normality in combustion–acoustic interaction in diffusion flames: a critical revision. *Journal of Fluid Mechanics*, 733:681–683, 2013.

[42] Jan Matheis and Stefan Hickel. Multi-component vapor-liquid equilibrium model for LES of high-pressure fuel injection and application to ECN Spray A. *International Journal of Multiphase Flow*, 99:294–311, 2018.

[43] KR McManus, Thierry Poinsot, and Sébastien M Candel. A review of active control of combustion instabilities. *Progress in Energy and Combustion Science*, 19(1):1–29, 1993.

[44] Emmanuel Motheau, Ann Almgren, and John B Bell. Navier–stokes characteristic boundary conditions using ghost cells. *AIAA Journal*, pages 3399–3408, 2017.

[45] Franck Nicoud and Thierry Poinsot. Thermoacoustic instabilities: Should the rayleigh criterion be extended to include entropy changes? *Combustion and Flame*, 142(1-2):153–159, 2005.

[46] Joseph C Oefelein. Thermophysical characteristics of shear-coaxial LOX–H2 flames at supercritical pressure. *Proceedings of the Combustion Institute*, 30(2):2929–2937, 2005.

[47] Gerald Pellett, Amy Kabaria, Babita Panigrahi, Katie Sammons, Janet Convery, and Lloyd Wilson. Dynamic weakening (extinction) of simple hydrocarbon-air counterflow diffusion flames by oscillatory inflows. In *41st AIAA/ASME/SAE/ASEE Joint Propulsion Conference & Exhibit*, page 4332, 2005.

[48] Ding-Yu Peng and Donald B Robinson. A new two-constant equation of state. *Industrial & Engineering Chemistry Fundamentals*, 15(1):59–64, 1976.

[49] N Peters. Laminar flamelet concepts in turbulent combustion. In *Symposium (International) on Combustion*, volume 21, pages 1231–1250. Elsevier, 1988.

[50] S Pohl, M Jarczyk, M Pfitzner, and B Rogg. Real gas CFD simulations of hydrogen/oxygen supercritical combustion. *Progress in Propulsion Physics*, 4:583–614, 2013.

[51] T Poinsot and SK Lele. Boundary conditions for direct simulations of compressible viscous flows. *Journal of computational physics*, 101(1):104–129, 1992.

[52] Thierry Poinsot and Denis Veynante. *Theoretical and numerical combustion*. RT Edwards, Inc., 2005.

[53] FRS Rayleigh. The explanation of certain acoustical phenomena. *Nature*, 18:319–321, 1878.

[54] Robert C Reid, John M Prausnitz, and Bruce E Poling. *The properties of liquids and gases*. McGraw-Hill, New York, 1987.

[55] Guillaume Ribert, Nan Zong, Vigor Yang, Laetitia Pons, Nasser Darabiha, and Sébastien Candel. Counterflow diffusion flames of general fluids: Oxygen/hydrogen mixtures. *Combustion and Flame*, 154(3):319–330, 2008.

[56] Takeo Saitoh and Yoshiro Otsuka. Unsteady behavior of diffusion flames and premixed flames for counter flow geometry. *Combustion Science and Technology*, 12(4-6):135–146, 1976.

[57] Jeffrey D Scargle. Studies in astronomical time series analysis. II. statistical aspects of spectral analysis of unevenly spaced data. *The Astrophysical Journal*, 263:835–853, 1982.

[58] K Seshadri and FA Williams. Laminar flow between parallel plates with injection of a reactant at high reynolds number. *International Journal of Heat and Mass Transfer*, 21(2):251–253, 1978.

[59] Camilo F Silva, Thomas Emmert, Stefan Jaensch, and Wolfgang Polifke. Numerical study on intrinsic thermoacoustic instability of a laminar premixed flame. *Combustion and Flame*, 162(9):3370–3378, 2015.

[60] Camilo F Silva, Malte Merk, Thomas Komarek, and Wolfgang Polifke. The contribution of intrinsic thermoacoustic feedback to combustion noise and resonances of a confined turbulent premixed flame. *Combustion and Flame*, 182:269–278, 2017.

[61] LL Smith, RW Dibble, L Talbot, RS Barlow, and CD Carter. Laser raman scattering measurements of differential molecular diffusion in turbulent nonpremixed jet flames of h2co2 fuel. *Combustion and flame*, 100(1-2):153–160, 1995.

[62] Giorgio Soave. Equilibrium constants from a modified redlich-kwong equation of state. *Chemical engineering science*, 27(6):1197–1203, 1972.

[63] CH Sohn and SH Chung. Effect of pressure on the extinction, acoustic pressure response, and no formation in diluted hydrogen–air diffusion flames. *Combustion and Flame*, 121(1-2):288–300, 2000.

[64] CH Sohn, SH Chung, SR Lee, and JS Kim. Structure and acoustic-pressure response of hydrogen–oxygen diffusion flames at high pressure. *Combustion and Flame*, 115(3):299–312, 1998.

[65] Chae-Hoon Sohn. Unsteady analysis of acoustic pressure response in N2 diluted H2 and air diffusion flames. *Combustion and flame*, 128(1-2):111–120, 2002.

[66] Warren C Strahle. Periodic solutions to a convective droplet burning problem: the stagnation point. In *Symposium (International) on Combustion*, volume 10(1), pages 1315–1325. Elsevier, 1965.

[67] Warren C Strahle. Unsteady laminar jet flame at large frequencies of oscillation. *AIAA Journal*, 3(5):957–960, 1965.

[68] Warren C Strahle. Unsteady reacting boundary layer on a vaporizing flat plate. *AIAA Journal*, 3(6):1195–1198, 1965.

[69] Warren C Strahle. High-frequency behavior of the laminar jet flame subjected to transverse sound waves. In *Symposium (International) on Combustion*, volume 11(1), pages 747–754. Elsevier, 1967.

[70] CJ Sung and Chung King Law. Structural sensitivity, response, and extinction of diffusion and premixed flames in oscillating counterflow. *Combustion and Flame*, 123(3):375–388, 2000.

[71] CJ Sung, JB Liu, and Chung King Law. Structural response of counterflow diffusion flames to strain rate variations. *Combustion and Flame*, 102(4):481–492, 1995.

[72] RHD Townsend. Fast calculation of the lomb-scargle periodogram using graphics processing units. *The Astrophysical Journal Supplement Series*, 191(2):247, 2010.

[73] Christoph Traxinger, Julian Zips, and Michael Pfitzner. Single-phase instability in non-premixed flames under liquid rocket engine relevant conditions. *Journal of Propulsion and Power*, pages 1–15, 2019.

[74] Hiroshi Tsuji. Counterflow diffusion flames. *Progress in Energy and Combustion Science*, 8(2):93–119, 1982.

[75] FA Williams. Theory of combustion in laminar flows. *Annual Review of Fluid Mechanics*, 3(1):171–188, 1971.

[76] J Xiao, E Austin, and WL Roberts. Relative polycyclic aromatic hydrocarbon concentrations in unsteady counterflow diffusion flames. *Combustion science and technology*, 177(4):691–713, 2005.

[77] MX Yao, J-P Hickey, PC Ma, and M Ihme. Molecular diffusion and phase stability in high-pressure combustion. *Combustion and Flame*, 210:302–314, 2019.

[78] AC Zambon and HK Chelliah. Self-sustained acoustic-wave interactions with counterflow flames. *Journal of Fluid Mechanics*, 560:249–278, 2006.

[79] Dan Zhao, Shen Li, and He Zhao. Entropy-involved energy measure study of intrinsic thermoacoustic oscillations. *Applied energy*, 177:570–578, 2016.

[80] Hao Zhou, Sheng Meng, Chengfei Tao, and Zihua Liu. Study of burner geometry effects on non-premixed flame response under acoustic excitation. *Journal of Low Frequency Noise, Vibration and Active Control*, 38(1):3–17, 2019.